ANNUAL REVIEWS

Annual Review of Fluid Mechanics

Dynamics of Flexible Fibers in Viscous Flows and Fluids

Olivia du Roure,[1] Anke Lindner,[1,2] Ehssan N. Nazockdast,[3] and Michael J. Shelley[4,5]

[1]Laboratoire de Physique et Mécanique des Milieux Hétérogènes (PMMH), ESPCI Paris, PSL University, CNRS, Sorbonne University, and Paris Diderot University, 75005 Paris, France; email: olivia.duroure@espci.fr

[2]Global Station for Soft Matter, Global Institution for Collaborative Research and Education, Hokkaido University, Sapporo 060-0808, Japan

[3]Applied Physical Sciences, University of North Carolina at Chapel Hill, North Carolina 27514, USA

[4]The Courant Institute of Mathematical Sciences, New York University, New York, NY 10012, USA

[5]Center for Computational Biology, Flatiron Institute, New York, NY 10010, USA

Annu. Rev. Fluid Mech. 2019. 51:539–72

The *Annual Review of Fluid Mechanics* is online at fluid.annualreviews.org

https://doi.org/10.1146/annurev-fluid-122316-045153

Keywords

flexible fibers, microfluidics, flow control, elasticity, buckling, hydrodynamics, complex fluids, suspensions

Abstract

The dynamics and deformations of immersed flexible fibers are at the heart of important industrial and biological processes, induce peculiar mechanical and transport properties in the fluids that contain them, and are the basis for novel methods of flow control. Here we focus on the low–Reynolds number regime where advances in studying these fiber–fluid systems have been especially rapid. On the experimental side, this is due to new methods of fiber synthesis, microfluidic flow control, and microscope-based tracking measurement techniques. Likewise, there have been continuous improvements in the specialized mathematical modeling and numerical methods needed to capture the interactions of slender flexible fibers with flows, boundaries, and each other.

1. INTRODUCTION AND BACKGROUND

An important class of microscale fluid–structure interactions involves the interactions and deformations of flexible fibers with fluid flows. This is evident in the many biological transport processes such as microorganismal swimming (Lauga & Powers 2009) or nuclear positioning in eukaryotic cells (Shelley 2016) that involve either actuated or passive flexible fibers. Fibers are the microstructures of many complex fluids, biological, industrial, and synthetic, studied both for their scientific and industrial importance and for their peculiar mechanical responses (Broedersz & MacKintosh 2014). Such suspensions are particularly challenging to study because the suspended fibers have many degrees of freedom in deformation and can exhibit microscopic instabilities. This makes the interaction of fibers with background flows surprisingly complex. Both anchored and freely suspended flexible fibers have recently been studied for purposes in microfluidic flow control, and when actuated, they can exhibit complex collective and transport dynamics.

This review focuses on the low–Reynolds number regime, as progress on fiber–fluid interactions in this regime has been especially rapid. On the experimental side, this is due to improvements in fiber synthesis and characterization, microfluidic flow control, and improved microscope-based measurement and particle tracking techniques. By taking advantage of the relative simplicity of the Stokes equations (as opposed to the Navier–Stokes equations), combined with adaptive resolution and fast summation approaches, there has been a similarly rapid improvement in numerical methods for simulating the deformations and interactions of fibers with flows, as well as with each other and other immersed structures. Coarse-grained descriptions of fiber assemblies and suspensions remain in their early stages, but their development is being sped by these new numerical methodologies.

In outline, we first discuss the current state-of-art in experimental synthesis and measurement techniques and in numerical methods for dynamical simulation of fiber–fluid interactions. We then describe the results of both experiment and theory for the dynamics of free and anchored fibers, followed by a review of the current state of research in many fiber–fluid systems. We close with a discussion of future directions.

Here we briefly introduce a few important physical parameters and relations. Consider a slender elastic fiber of length L, of circular cross section with radius a (hence, $\epsilon = a/L \ll 1$), and of flexural rigidity $E = YI$, where Y is the material Young's modulus and I is the areal moment of inertia ($I = \pi a^4/4$). This fiber is immersed in a Newtonian fluid of shear viscosity μ with the fluid motion characterized by a strain rate $\dot{\gamma}$. Neglecting inertial forces, three important forces are at play: Brownian forces $\sim k_B T/L$ (k_B is the Boltzmann constant and T is the temperature), drag forces $\sim \mu\dot{\gamma}L^2$, and elasticity forces $\sim E/L^2$. For most of the work reviewed here, though not all, viscous drag and elasticity forces dominate Brownian forces. This predominance requires that ℓ_p/L and $Pe = 8\pi\mu\dot{\gamma}L^3/k_B T$ be significantly greater than 1, where $\ell_p = E/k_B T$ is the persistence length of the fiber against thermal fluctuations, and the Péclet number, Pe, is the ratio of viscous to Brownian forces. Taking water as the solvent, a fluid strain rate of $\dot{\gamma} = 1\ s^{-1}$, and a fiber length of $L = 4\ \mu m$, we have $Pe \sim 400$. For fibers of a length greater than a few microns, Pe is much greater than 1 and the center of mass diffusion can thus always be neglected compared to advection by viscous flow. Now, for a material modulus of $Y = 1$ GPa and an aspect ratio of $\epsilon = 10^{-2}$, we find $\ell_p/L \sim 10^5$ and Brownian forces can be neglected over elastic forces. This is the case for most of the synthetic fibers treated in this review. Decreasing the aspect ratio to $\epsilon = 10^{-3}$ and decreasing Y by an order of magnitude reduces ℓ_p/L to $\ell_p/L \sim 1$, and shape fluctuations resulting from Brownian forces will become important. This is the case for semiflexible polymers as well as actin filaments, for example. Finally, while this dimensionless parameter appears naturally later in the review, we introduce here $\tilde{\eta} = 8\pi\mu\dot{\gamma}L^4/Ec$, where $c = -\ln(e\epsilon^2)$ is the ratio between viscous and elastic forces, a control parameter in many fiber–fluid problems.

2. EXPERIMENTAL TECHNIQUES

A limiting factor in fiber–fluid interaction experiments is achieving good control of fibers in terms of their shapes, dimensions, and mechanical properties, as well as good control of the flow geometry. Even if low–Reynolds number experiments can be carried out at macroscopic scales by using highly viscous suspending fluids, it is much more comfortable and advantageous to work at microscopic scales, where optical microscopy and microfluidics can be combined to perform reliable experiments. The microscopic approach requires microfabrication techniques, smart choices regarding the microchannel geometry, and ways to track the particle and its deformation while transported. All of these aspects are detailed in the following discussion.

2.1. Fiber Synthesis and Properties

Reliable experiments require fibers that have controlled dimensions and high aspect ratios, as well as known and reproducible mechanical properties. Recent fabrication techniques that can be directly implemented into the channels are specially well suited for this goal.

2.1.1. Fiber fabrication. The fabrication of microparticles with nonspherical shapes has received much attention in recent years, but elongated objects require specific approaches. Electrospinning can be an efficient technique to fabricate fibers of typical diameters of ∼200 nm and lengths of 1–100 μm (**Figure 1*i***) with controlled mechanical properties (Li & Xia 2004, Jun et al. 2014, Nakielski et al. 2015). Microfluidics has opened new routes to tailor elongated objects. Controlling the channel geometry, one can form a jet of a solution that will solidify either by photopolymerization or by diffusion of small molecules from the surrounding fluid (**Figure 1*a*,*b***) (Jeong et al. 2004, Mercader et al. 2010, Choi et al. 2011, Nunes et al. 2012, Perazzo et al. 2017). Another option is to photopolymerize a photosensitive solution directly in the microchannel through a mask that determines the object shape (**Figure 1*c–e***). The presence of oxygen close to the polydimethylsiloxane walls prevents polymerization in these regions, keeping the fabricated object free to flow in the microchannel (Helgeson et al. 2011, Berthet et al. 2016). Finally, self-assembly of colloids is a reliable technique that produces very flexible, high–aspect ratio particles, but their sedimentation due to their high density can be limiting (**Figure 1*b***) (Goubault et al. 2005, Zhang et al. 2011, Berthet et al. 2016).

Another attractive strategy is to rely on biology for controlled and monodisperse elongated objects. Actin filaments, semiflexible polymers resulting from the polymerization of globular protein, are models for flexible Brownian fibers (Harasim et al. 2013, Kirchenbuechler et al. 2014, Liu et al. 2018). Microtubules are another candidate. Bacterial colonies can also form elongated objects that allow fluid–structure interaction problems to be studied (Rusconi et al. 2010, 2011; Amir et al. 2014).

More complex shapes can be produced. In two dimensions, approaches based on self-assembly or photolithography can be implemented (**Figure 1*c–e***) (Li & Xia 2004). Three-dimensional (3D) fabrication is more challenging, and attention has focused on microhelices given their similarity to bacterial flagellae. Electrospinning is a widespread technology (reviewed by Silva et al. 2017); the spontaneous formation of helices from flat ribbons is an elegant alternative (**Figure 1*f***) (Pham et al. 2013). Recent developments in 3D printing using two-photon excitation allow for submicron resolution but are currently limited to rigid objects (**Figure 1*g***).

2.1.2. Mechanical characterization. The mechanical properties of macroscale fibers can be measured by rheometry or by the bending of the fiber under its own weight (**Figure 1*j***). When

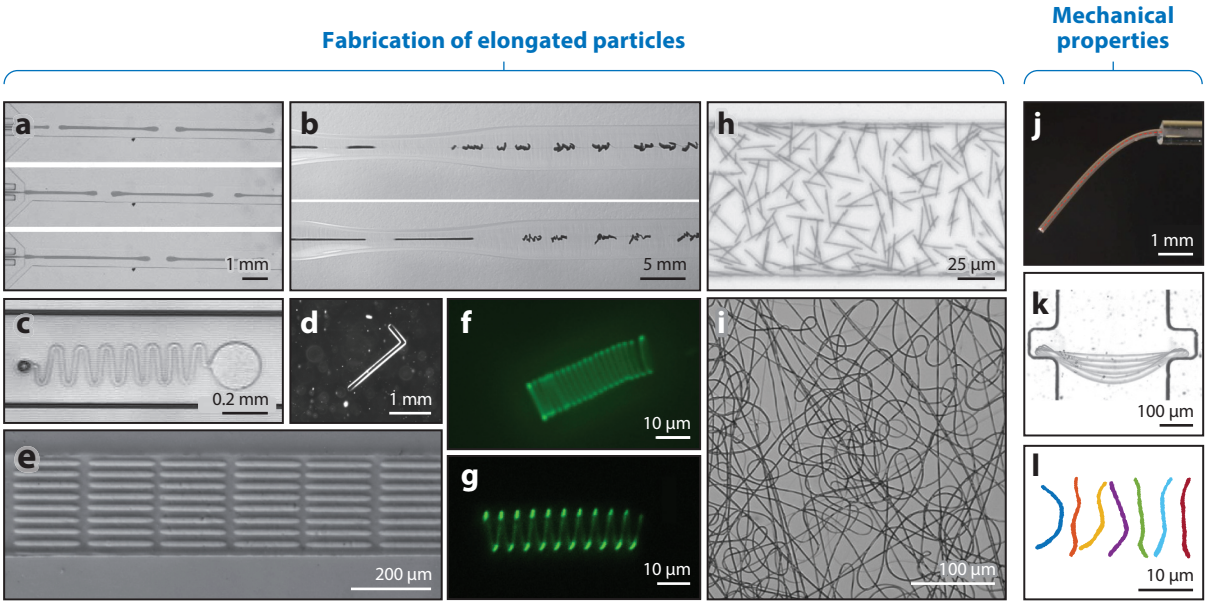

Figure 1

Fibers, their fabrications, and their mechanical properties. (*a*,*b*) Particles directly fabricated in microfluidic channels: Jets are polymerized by either (*a*) light or (*b*) chemicals. (*c*–*e*) Particles synthesized in a microchannel by photopolymerization of a photosensitive solution through a mask. (*f*) A flexible helix spontaneously formed from an asymmetric ribbon. (*g*) A microprinted helix. (*h*) A magnetic fiber suspension fabricated by self-assembly of magnetic colloids. (*i*) Electrospun fibers. (*j*–*l*) Characterization of mechanical properties: (*j*) bending of a macroscopic fiber under its own weight, (*k*) superimposed shapes of a photopolymerized fiber deformed by increasing flow rates, and (*l*) bending fluctuations of an actin filament. Panels adapted from or provided by (*a*) Nunes et al. (2012), (*b*) Mercader et al. (2010), (*c*) Attia et al. (2009), (*d*) J. Cappello and M. Daïeff, (*e*,*h*) Berthet et al. (2016), (*f*) M. Daïeff, (*g*) F. Tesser and J. Laurent, (*i*) Nakielski et al. (2015), (*j*) Quennouz (2013), and (*k*) Duprat et al. (2015), and (*l*) Y. Liu. All panels reprinted with permission.

working with elastomers, these two measurements are in good agreement (Quennouz et al. 2015). Beam-bending measurements can be implemented in a microfluidic channel to perform in situ measurements (**Figure 1*k***) (Duprat et al. 2015).

When the smallest dimension of the fiber is a micron or less, Brownian fluctuations can be large enough to induce bending deformations. In this case, the flexural rigidity E can be expressed as $\ell_p k_B T$, where ℓ_p is the persistence length, and an elegant way to measure E is to extract ℓ_p from the analysis of many filament configurations (**Figure 1*l***). This approach is common for biological semiflexible polymers like actin or microtubules (Gittes et al. 1993) and has also been used for tiny electrospun filaments (Nakielski et al. 2015).

2.2. Flow Control

At large spatial scales, working at low Reynolds numbers requires long-time experiments with low-velocity flows of highly viscous liquids. However, at small scales, low Reynolds numbers are easily achievable even with low-viscosity fluids. For this regime, the channel geometry completely determines the flow, and thus different flows can be obtained depending on the device design.

To avoid flow complexity, researchers often perform studies using linear extensional or shear flows (**Figure 2*a*,*b***). Experimentally, working with linear shear flow is only possible in a Couette geometry if the gap is small compared to the cylinder's diameter (**Figure 2*a***). In channel flows,

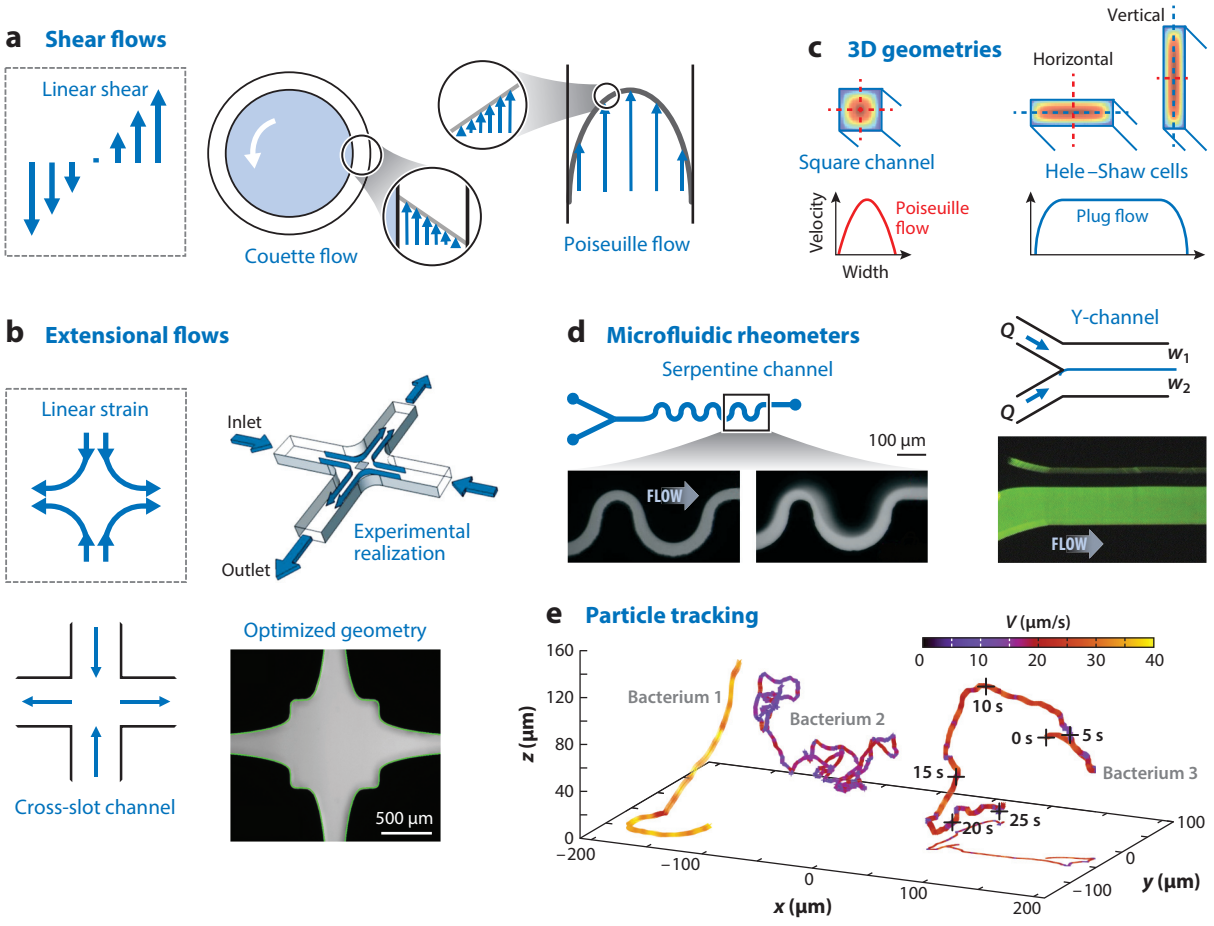

Figure 2

Flow control and fiber tracking. Geometries for (*a*) shear and (*b*) extensional flows. (*a*) The velocity profile of linear shear and schematics of Couette flow and Poiseuille flow in a channel that locally approximates linear shear. (*b*) The velocity profile of linear strain, a schematic of a cross-slot channel, an experimental realization (image adapted with permission from Kantsler & Goldstein 2012), and an optimized cross-slot geometry giving a larger area with constant extension rate (image adapted with permission from Haward et al. 2012). (*c*) Flow geometries in three dimensions. A square channel and vertical and horizontal Hele–Shaw cells. Velocity profiles corresponding to a Poiseuille flow (*red*) and a plug flow (*blue*) are shown. (*d*) Microfluidic rheometers. (*Left*) Serpentine channels can be used to study viscoelastic properties of non-Newtonian fluids. Photos adapted with permission from Zilz et al. (2014). (*Right*) Y-channels are well suited to measure shear viscosities with high resolution. Photo adapted with permission from Galambos & Forster (1998). (*e*) Lagrangian tracking of bacteria in a microchannel. Panel adapted with permission from Darnige et al. (2017).

linear shear can be approximated by Poiseuille flow if the object size is much smaller than the channel height (**Figure 2*a***) (Liu et al. 2018). Cross-slot geometries generate extensional flows but with small spatial extension. An elegant but difficult way of overcoming this limitation is to keep the object at the stagnation point by adjusting the pressures in the different entries, as was implemented by Schroeder et al. (2003) and later by Kantsler & Goldstein (2012) (see **Figure 2*b***). A more robust way is to numerically optimize the exact geometry to obtain a purely extensional flow over a larger distance even in the presence of the walls (**Figure 2*b***) (Haward et al. 2012, Zografos et al. 2016).

Numerical simulations are sometimes done in two dimensions due to their relative simplicity, while in experiments, 2D flows are not always easy to achieve. One option is to use a Hele–Shaw geometry, in which lateral dimensions are much larger than the cross-channel dimension (**Figure 2*c***). On a microscope, the vertical configuration allows a nearly 2D flow to be generated in the observation plane above the boundary (Haward et al. 2012).

Flows can be controlled by syringe pumps imposing flow rates or by pressure control devices. Pressure control is well adapted to low velocity and low shear rates. Particle velocimetry techniques are used to quantitatively determine local velocities and thus shear rates.

Microfluidic rheometers are new developments in the field that access the rheological properties of complex suspensions of various types (**Figure 2*d***) (Lindner & Arratia 2016). Their main advantages are their sensitivity to low variations in viscosity and normal stresses and the possibility of directly observing the flowing particles within the device.

2.3. Particle Observations and Tracking

Typically, fiber deformations and trajectories need to be measured simultaneously even though they occur at different spatial scales: Images with high magnification are necessary to obtain a good resolution of fiber deformations, whereas trajectories are inherently large scale. In a microchannel, a bright field, phase contrast, and fluorescence microscopy are usually best suited to obtain images of fiber deformations of a sufficient quality. The use of high-magnification and high–numerical aperature objectives is in general required. In addition, a long working distance can be very useful for observing filaments far from the bottom of the chamber where the coupling to the wall is negligible. At macroscale, the 3D shape may be reconstructed from images taken by two cameras or by the smart use of mirrors.

To track an object along its trajectory at the macroscale, one automates the motion of the camera. Keeping a fiber in the field of view in a microfluidic channel requires that the microscope stage move at or near the fiber velocity. In combination with a fast camera, this avoids image blurring. Following trajectories in three dimensions becomes necessary when objects do not follow streamlines, as in cross-stream migration, or for active particles. In this case, one can use 3D tracking algorithms like those developed for following swimming bacteria (Darnige et al. 2017, Qu et al. 2018).

3. MATHEMATICAL MODELING AND SIMULATION METHODS

The interaction of flexible fibers with Stokesian fluids has a special structure for which specialized mathematical and computational methods have been developed. The most basic is local slender body theory (SBT), which gives a leading-order local relation between elastic and drag forces and is a mainstay for analysis. Nonlocal interactions arising from fluid incompressibility can be captured through the use of higher-order, and more complex, slender body formulations or through other approaches such as immersed boundary methods (IBM), bead–rod models, or regularized Stokeslet methods. Here, we first discuss the nonlocal SBT formulation, as it is compact and amenable to fast solution methodologies.

3.1. Nonlocal Slender Body Theory

The appeal of nonlocal SBT is its reduction of filament–fluid and filament–filament interactions to relatively simple dynamic equations for filament centerlines. For this, we assume that the fluid

is described by the incompressible Newtonian Stokes equation,

$$\mu\Delta\mathbf{u} - \nabla p = \mathbf{0} \quad \text{and} \quad \nabla\cdot\mathbf{u} = 0, \tag{1.}$$

where μ is the shear viscosity, $\mathbf{u}$ is the fluid velocity, and p is the pressure. Generally, solutions to the Stokes equations can be found using boundary integral methods (Pozrikidis 1992), where the fluid velocity is represented as a distribution of fundamental solutions to the Stokes equations on all immersed and bounding surfaces. The fundamental solution corresponding to a δ-function of force is given by the Stokeslet tensor, $\mathbf{G}(\mathbf{x}) = \frac{1}{8\pi\mu}\frac{\mathbf{I}+\hat{\mathbf{x}}\hat{\mathbf{x}}}{|\mathbf{x}|}$, for $\hat{\mathbf{x}} = \mathbf{x}/|\mathbf{x}|$.

The flows produced by the motion of slender fibers can be treated especially. One approach assumes that such flows arise from distributions of Stokeslet singularities along fiber centerlines and uses techniques of matched asymptotics (in fiber slenderness ratio) to determine the unknown singularity densities (Keller & Rubinow 1976, Johnson 1980, Götz 2000). Another approach derives such reductions to the centerline directly from a full singular surface integral formulation of the problem, again using slenderness ratio as an asymptotic parameter (Sellier 1999, Koens & Lauga 2018). These reductions are the basis for efficient numerical simulation of slender fiber dynamics. Specifically, consider N fibers, each of radius a and lengths L_n, with centerline positions $\mathbf{X}^n(s,t)$ for $n = 1,\ldots,N$, where s is the arclength ($0 \le s \le L_n$). Each fiber is assumed to be slender, i.e., $\epsilon_n = a/L_n \ll 1$, and to exert a force per unit length $\mathbf{f}^n(s,t)$ on the surrounding fluid. Given a background flow $\bar{\mathbf{u}}$, the fluid velocity at a point $\mathbf{x}$ within the fluid is, to leading order, given by a distributions of Stokeslets along fiber centerlines:

$$\mathbf{u}(\mathbf{x}) = \mathbf{u}_{\mathrm{F}}(\mathbf{x}) + \bar{\mathbf{u}}(\mathbf{x}), \quad \text{where} \quad \mathbf{u}_{\mathrm{F}}(\mathbf{x}) = \sum_{m=1}^{N}\int_0^{L_m} \mathbf{G}[\mathbf{x}-\mathbf{X}^m(s')]\cdot\mathbf{f}^m(s')\,\mathrm{d}s'. \tag{2.}$$

Götz (2000) derives higher-order corrections in terms of integrals of Stokes doublets.

The self-induced velocity of a fiber is not found by direct evaluation of Equation 2 upon that fiber. This yields a logarithmically divergent integral. Instead, fiber self-induction is a matter of careful asymptotic matching (Keller & Rubinow 1976, Johnson 1980, Götz 2000). Such analyses give the velocity of the centerline $\mathbf{X}^n(s)$ as

$$\mathbf{V}^n(s) = \bar{\mathbf{u}}(\mathbf{X}^m) + \sum_{m=1,m\neq n}^{N}\mathbf{u}^m_{\mathrm{F}}(\mathbf{X}^n) + \frac{1}{8\pi\mu}\left[c_n\left(\mathbf{I}+\mathbf{X}^n_s\mathbf{X}^n_s\right)\mathbf{f}^n + \mathbf{K}_n[\mathbf{f}^n]\right], \tag{3.}$$

where $\mathbf{X}_s$ is the tangent vector and the subscript s denotes a partial derivative. Here, $c_n = -\ln(\epsilon_n e^2)$ is an asymptotically large parameter, and $\mathbf{K}_n$ is an $\mathcal{O}(\epsilon^0)$ linear operator that contains a finite-part integral of Stokeslets that captures fiber self-interactions. The use of this integral in computation is discussed by Tornberg & Shelley (2004), who showed that it must be appropriately regularized both to maintain asymptotic accuracy and to control the growth of short-wavelength modes treated inaccurately by SBT.

Equation 3 relates the fiber velocity to the fiber forces acting upon the fluid. As a dynamics problem, this system is closed by specifying the fiber elastic forces and identifying a Lagrangian or material variable for the fiber. These are done simultaneously by modeling each fiber as an inextensible Euler–Bernoulli beam,

$$\mathbf{f}^n = \mathbf{f}^n_{\mathrm{E}} = -E\mathbf{X}^n_{ssss} + (T^n\mathbf{X}^n_s)_s,\ 0 \le s \le L_n, \tag{4.}$$

where $-E\mathbf{X}_{ssss}$ is the bending force per unit length, T is the axial tension, and $(T\mathbf{X}_s)_s$ is the tension force per unit length. Inextensibility identifies s as a material variable, and hence we have $\mathbf{X}^n_t(s,t) = \mathbf{V}^n$. Inextensibility also generates an auxiliary integro-differential equation for T by

imposing $\mathbf{V}_s^n \cdot \mathbf{X}_s^n = 0$, which follows from differentiating the identity $\mathbf{X}_s^n \cdot \mathbf{X}_s^n = 1$ (Tornberg & Shelley 2004).

3.2. The Special Case of Local Slender Body Theory

Local SBT has been the mainstay for theoretical analyses of the dynamics of flexible fibers, and it sits at the core of many numerical approaches. In particular, retaining from Equation 3 only the logarithmic leading order in ϵ, we have a local balance of fluid drag forces and fiber forces exerted on the fluid,

$$\mathbf{R}(s,t) \cdot [\mathbf{V}(s,t) - \bar{\mathbf{u}}(\mathbf{X}(s,t),t)] = \mathbf{f}(s,t), \qquad 5.$$

for $\mathbf{R} = \eta\,(\mathbf{I} - \mathbf{X}_s\mathbf{X}_s/2)$ and $\eta = 8\pi\mu/c$. For an elastic fiber modeled by Equation 4, we have a dynamical equation plus a constraint:

$$\mathbf{X}_t = \mathbf{V} \equiv \mathbf{u}(\mathbf{X},t) + \eta^{-1}(\mathbf{I} + \mathbf{X}_s\mathbf{X}_s)\,[-E\mathbf{X}_{ssss} + (T\mathbf{X}_s)_s] \quad \text{and} \quad \mathbf{X}_s \cdot \mathbf{V}_s = 0. \qquad 6.$$

The inextensibility constraint generates an elliptic equation for T,

$$2T_{ss} - |\mathbf{X}_{ss}|^2 T = S, \qquad 7.$$

where S depends upon background flow and the bending force. Given appropriate boundary conditions, T has a unique solution, and Equation 6 can be used to evolve the fiber's shape, position, and orientation.

3.2.1. Basic scaling. Consider a background flow with a characteristic length scale W and timescale $\dot{\gamma}^{-1}$, expressed as $\bar{\mathbf{u}} = \dot{\gamma} W \mathbf{U}(\mathbf{x}/W, \dot{\gamma}t)$. By scaling space on L, time on $\dot{\gamma}^{-1}$, and tension T on E/L^2, Equation 6 can be given in nondimensional form as

$$\mathbf{V} = \alpha^{-1}\mathbf{U}(\alpha\mathbf{X},t) - \tilde{\eta}^{-1}(\mathbf{I} + \mathbf{X}_s\mathbf{X}_s)\,[\mathbf{X}_{ssss} - (T\mathbf{X}_s)_s]\,, \qquad 8.$$

with $\alpha = L/W$, and where $\tilde{\eta} = 8\pi\mu\dot{\gamma}L^4/Ec$ is the effective strength of flow forcing. Note that for linear background flows, α disappears from the equation. If the tension is negative, reflecting compressive fluid stresses, then Equation 8 is seen as a competition of fourth-order diffusion and second-order antidiffusion.

3.2.2. Boundary conditions. Finally, boundary conditions are needed on the tensile and bending forces. For freely suspended fibers, these are the natural boundary conditions of having zero applied forces and torques, which simplify to $\mathbf{X}_{sss} = \mathbf{X}_{ss} = \mathbf{0}$ and $T = 0$ on each end of the fiber. These boundary conditions are natural given that the fiber force contains $\mathbf{X}_{ssss}$ (and hence needs two boundary conditions at each end) and that T satisfies an elliptic boundary value problem (and so needs one boundary condition at each end). Having filaments attached (clamped or hinged) to surfaces, mobile or immobile, generates other boundary conditions and explores other dynamics, as detailed in Nazockdast et al. (2017b).

3.3. Brownian Semiflexible Fibers

Thus far, we have assumed the fibers to be rigid enough that thermal fluctuations have a negligible effect upon their conformations. For this to hold, the length of the fibers needs to be significantly smaller than their persistence length ℓ_p. If this assumption is not met (as can be for carbon nanotubes, actin filaments, and worm-like polymers), thermal fluctuations can have important consequences on the overall mechanics of the suspension, and they have been the subject of many

studies. A review of this topic is beyond the scope here, and we refer the interested reader to Broedersz & MacKintosh (2014). Here we only give a limited summary of previous work and the outstanding challenges.

In the presence of thermal fluctuations, Equation 5 is modified to

$$\mathbf{R} \cdot (\mathbf{X}_t - \bar{\mathbf{u}}) = -E\mathbf{X}_{ssss} + (T\mathbf{X}_s)_s + \mathbf{f}^{\mathrm{B}}(s), \qquad 9.$$

where $\mathbf{f}^{\mathrm{B}}$ is the thermal fluctuating force with zero mean and a finite variance given by the fluctuation dissipation theorem:

$$\langle \mathbf{f}^{\mathrm{B}}(s,t) \rangle = \mathbf{0} \quad \text{and} \quad \langle \mathbf{f}^{\mathrm{B}}(s,t)\mathbf{f}^{\mathrm{B}}(s',t') \rangle = 2kT\mathbf{R}(s,t)\delta(s-s')\delta(t-t'). \qquad 10.$$

The brackets denote ensemble averages. Munk et al. (2006) used this formulation to study a 2D Brownian semiflexible fiber in shear flow. Manikantan & Saintillan (2013) also used this formulation in studies of Brownian flexible fibers in 2D arrays of counterrotating Taylor–Green vortices and extensional flows.

It follows from Equation 10 that computing the displacements from thermal fluctuations requires computing $\mathbf{R}^{1/2}$. For local SBT, $\mathbf{R}^{1/2}$ can be computed analytically. For nonlocal SBT, the resistance tensor, $\mathbf{R}$, is nonlocal and depends on the position of all fibers. Numerically, this means computing the square root of a $P \times P$ matrix, where $P = 3N \cdot M$ and M is the number of discretization points per fiber. The direct computation of $\mathbf{R}^{1/2}$ requires $\mathcal{O}(P^3)$ operations, which makes simulation of systems beyond a few fibers very expensive. More efficient techniques have been proposed to reduce the computational cost to P^α, with α varying between 1 and 2 depending on the conditions. In a recent development, Fiore et al. (2017) used Ewald summation to reduce the computational cost to $\mathcal{O}(P)$.

Several other works have modeled Brownian filaments by using bead–rod/bead–spring models for inextensible polymeric filaments. The main complexity involves imposing the inextensibility constraint. Specifically, it turns out that very stiff springs and inextensible rods differ in their degrees of freedom and hence in the resulting equilibrium statistical mechanics (Fixman 1978). Hinch (1994) showed that a psuedo-potential force needs be applied to a connection with a very stiff spring in order to exactly recover the behavior and statistical physics of an inextensible connection.

3.4. Fast Numerical Methods for Slender Body Theory

Tornberg & Shelley (2004) developed a stable and numerically tractable version of nonlocal SBT for flexible filaments with free ends and devised specialized quadrature schemes for the regularized finite-part integral in $\mathbf{K}[\mathbf{f}]$ of Equation 3. The fibers' centerlines were discretized uniformly and derivatives were evaluated using a second-order accurate finite difference scheme, while the trapezoidal rule was used for evaluating the remaining integrals. For time-stepping, a backward differentiation finite difference scheme was used, and the bending forces were treated implicitly to remove temporal stiffness, while the tension equation, which imposed inextensibility of the fibers, was treated explicitly.

Nazockdast et al. (2017b) extended the work of Tornberg & Shelley (2004) to a platform suitable for simulating a substantially larger number of fibers, $\mathcal{O}(1{,}000)$ or more. They used a Chebyshev basis for the representation of fiber position and to compute high-order derivatives with spectral accuracy. They used implicit–explicit time discretization and treated both bending and tensile forces implicitly. As a result, they observed a three-orders-of-magnitude improvement in the maximum stable time step in their numerical experiments, as compared to the explicit treatment of tension by Tornberg & Shelley. They solved the linearized system of equations using the generalized minimal residual method (Saad & Schultz 1986) with a Jacobi or block Jacobi

preconditioner. A kernel-independent fast multipole method was utilized for fast computation of nonlocal hydrodynamic interactions (HIs) via fast matrix–vector products, yielding a computational cost of $\mathcal{O}(M)$ operations per time step, where M is the number of unknowns. The entire computational scheme was parallelized and scalable to many computational cores, which allowed the simulation of $\mathcal{O}(1{,}000)$ semiflexible filaments.

3.5. The Regularized Stokeslet Method

A popular method for solving the Stokes equations is Cortez's (2001) method of regularized Stokeslets, which uses superpositions of regularized fundamental solutions. Flores et al. (2005) used a superposition of regularized Stokeslets and rotlets to simulate the dynamics of driven flagellae. In their study, a flagellum is a network of flexible springs, and a helical shape so composed is driven by a torque at its base. In a study also modeling flagellae (and cilia), Smith (2009) developed a version of regularized Stokeslets that utilizes a boundary element approach to the discretization and incorporated the presence of walls (see also Jiang et al. 2014). Bouzarth et al. (2011) used a regularized representation of a 1D curve of 2D Stokeslets to simulate the nonlocal dynamics of flexible, slightly extensible fibers. Olson et al. (2013) have combined the regularized Stokeslet method for evolving slender rods with the internal mechanics of an elastica with intrinsic twist and curvature. And, in theoretical work, Cortez & Nicholas (2012) have developed an asymptotically consistent SBT based on regularized centerline forces.

3.6. The Immersed Boundary Method

Peskin's (2002) IBM has also been applied to this class of problems. In this method, a filament is discretized by Lagrangian markers connected by spring elements, and their relative displacements by fluid motions are used to calculate the filament's elastic response. These elastic forces are then distributed onto a background grid covering the fluid volume and are used as forces acting upon the fluid, thus modifying the fluid flow that displaces the markers (Lim & Peskin 2004). The advantage of IBM is that detailed immersed mechanical structures can be simulated, but at the cost of having to solve the flow equations in the entire fluid volume. Other volume-based methods have also been used in this context, including finite element/volume methods (Mitran 2007) and lattice Boltzmann methods (Wu & Aidun 2010).

Within the immersed boundary framework, for a fiber to have a physical width, the volume grid size needs to be several times smaller, making the method computationally expensive for simulating slender bodies such as fibers and thin disks. To overcome this, Nguyen & Fauci (2014) employed an adaptive mesh version of IBM (Griffith et al. 2007) to study the dynamics of flexible fibers as models, in part, of diatom chains (diatoms are unicellular phytoplankton). For this, they constructed fibers that are composite structures made of alternating segments that mimic the structure of diatom chains (see Section 4.1.2). While a simple inextensible beam model, like Equation 8, describes well the bending deformations of these composite structures, it does not model well their responses to compressive loads. Wiens & Stockie (2015) used their parallel implementation of IBM to simulate a suspension of up to 256 semiflexible fibers in shear flow. Their analysis of parallel performance shows that their algorithm is weakly scalable. Recently, Stein et al. (2017) implemented a fourth-order accurate IBM for studying flows over arbitrary smooth domains. A combination of this approach with adaptive gridding (see Griffith et al. 2007) might improve the computational efficiency and accuracy of the IBM in simulating slender objects such as fibers.

3.7. Bead–Rod Models

While closely related to methods based on SBT or IBM, bead–rod models have a somewhat independent lineage. In bead–rod models, a flexible fiber is represented as a 1D chain of linked rigid bodies (e.g., spheres, spheroids, rods) that experience local drag and interact with each other through short-range forces (e.g., repulsion, lubrication, friction), while sometimes neglecting long-ranged HIs or only including a subset of them. A recent review of these methods is given by Hämäläinen et al. (2011). In recent work, Delmotte et al. (2015) elaborated upon basic bead models by introducing a new Lagrange multiplier method to impose constraints and considered several flow problems (Jeffery orbits, buckling in shear, and actuated swimming filaments) by using an approximate accounting of Stokesian hydrodynamics.

4. FREE FIBERS IN FLOW

How fibers are buckled by flow is central to much of the interesting nonlinear dynamics observed in simulations and experiments of fiber motion. Here, we first discuss a prototypical situation—a straight fiber moving in a linear straining background flow—where buckling arises as an instability. We then discuss other prototypical problems, such as morphological transitions of fibers transported in linear shear flows and more complex flow geometries where the coupling of fiber deformation and transport can be observed.

4.1. Fiber Morphology in Simple Flows

Here we discuss the shape dynamics of fibers in linear shearing and straining flows.

4.1.1. Buckling instabilities in compressive flows. Because of its simplicity, local SBT is usually the preferred tool for studying linear stability of immersed fibers and is used here to illustrate the buckling instability of free fibers in the simplest of cases.

A perfectly straight isolated fiber will remain straight in any incompressible and linear flow, even as the fiber is translated and rotated. Hence, consider the background flow $\mathbf{U}(\mathbf{x}, t) = \mathbf{A}(t) \cdot \mathbf{x}$ with $\mathrm{tr}(\mathbf{A}) = 0$. A straight fiber can be represented as $\mathbf{X}(s, t) = \mathbf{X}_c(t) + s\mathbf{e}(t)$, where $\mathbf{X}_c$ is its center point, and $\mathbf{e}$ is a unit orientation vector. Inserting this form into Equations 8 and 7 and applying the natural conditions of zero total force and torque yield

$$\dot{\mathbf{X}}_c = \mathbf{A}\mathbf{X}_c, \quad \dot{\mathbf{e}} = (\mathbf{I} - \mathbf{e}\mathbf{e}^T)\mathbf{A}\mathbf{e}, \quad \text{and} \quad \bar{T} = -\frac{\tilde{\eta}}{4}(\mathbf{e}^T\mathbf{E}\mathbf{e})(s^2 - 1/4), \tag{11.}$$

where $\mathbf{E} = (\mathbf{A} + \mathbf{A}^T)/2$ is the symmetric rate of strain tensor. Hence, the rod center is carried with the local flow, the orientation vector obeys Jeffrey's equation (Jeffrey 1922), and the tension $\bar{T}$ is quadratic in s^2 with its sign determined by the orientation of $\mathbf{e}$ relative to the principle axes of $\mathbf{E}$. Thus, if the fiber is aligned with compressive straining of the flow, then the tension is negative and hence compressive. This is the condition required for a buckling instability.

The most straightforward case is given by a simple straining flow, $\bar{\mathbf{u}} = (x, -y)$, where the straight fiber is aligned with the y-axis (i.e., $\mathbf{e} \equiv \hat{\mathbf{y}}$). This choice maximizes flow compression (Young & Shelley 2007) and is free of explicit time dependance from the background flow. This leads to a variable coefficient eigenvalue problem for the growth or decay of an in-plane perturbation w to the straight fiber,

$$\sigma w = w + sw_s + \frac{1}{4}\left(s^2 - 1/4\right) w_{ss} - \tilde{\eta}^{-1} w_{ssss}, \tag{12.}$$

with $w_{ss} = w_{sss} = 0$ at $s = \pm 1/2$. With an eigenvalue solver, we can track the system's eigenvalues and eigenfunctions as the effective viscosity or strain rate, $\tilde{\eta}$, increases. For small $\tilde{\eta}$, the straight fiber is stable to perturbations. With an increase in $\tilde{\eta}$, we find the successive crossing to the right half-plane of eigenvalues coupled to eigenfunctions associated with increasingly higher-order bending modes. The first three crossings occur at $\tilde{\eta}_1 = 153.2$, $\tilde{\eta}_2 = 774.3$, and $\tilde{\eta}_3 = 1{,}930$ (Quennouz et al. 2015), and their associated eigenfunctions are shown in subpanel *i* of **Figure 3*a***. The respective eigenshapes are the classical U-, S-, and W-shaped buckling modes.

In experiments, it is nontrivial to achieve a linear straining flow and reasonably long residence times for a fiber moving in it. One possibility is to use the approach of a fiber at a stagnation point.

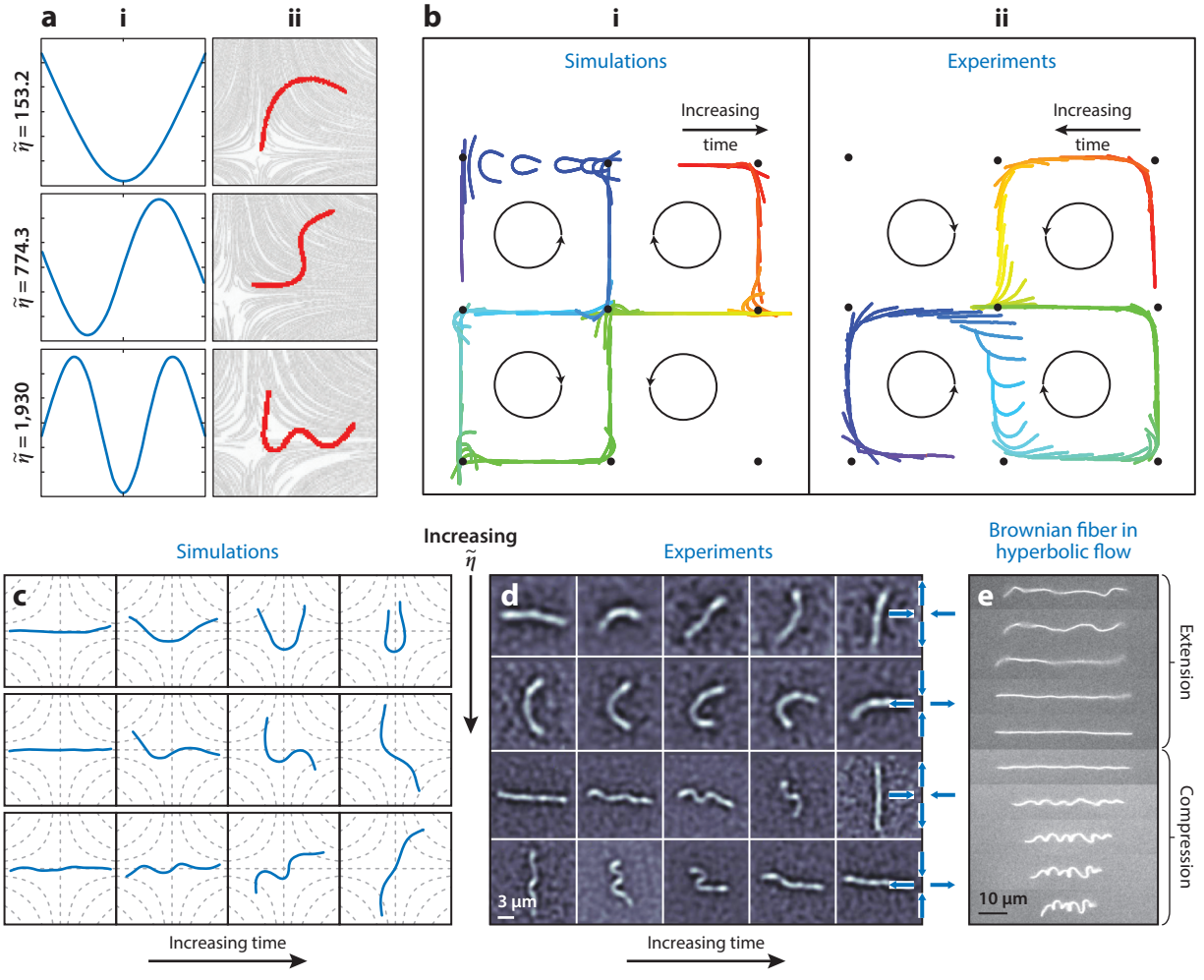

Figure 3

Fiber buckling. (*a*) Critical values of the control parameter $\tilde{\eta}$ and fiber shapes of buckling modes from (*i*) linear stability analysis and (*ii*) experiments. (*b*) A flexible fiber evolving in an array of hyperbolic stagnation points, $\tilde{\eta} \approx 2{,}000$, showing (*i*) simulations using slender body theory (SBT) and (*ii*) experiments with a centimetric polymeric fiber. (*c*,*d*) A Brownian fiber maintained at a stagnation point. (*c*) Numerical simulations using SBT. (*d*) Experiments using actin filaments in a microfluidic device. (*e*) An actin filament transported in a converging/diverging hyperbolic microchannel experiencing elongation followed by compression at $\tilde{\eta} = 7.9 \times 10^5$. Panels adapted from or provided by (*a*,*b*) Quennouz et al. (2015), (*c*) Manikantan & Saintillan (2015), (*d*) Kantsler & Goldstein (2012), and (*e*) Y. Liu. All panels reprinted with permission.

Wandersman et al. (2010) investigated fiber buckling in a macroscopic realization of such a system using centimetric soft elastomer fibers. These fibers move in a viscous quasi-2D cellular flow, an array of counterrotating vortices surrounding hyperbolic stagnation points. Above a critical value of $\tilde{\eta}$, fibers are observed to buckle (**Figure 3*b***, subpanel *ii*) at or near stagnation points. With increasing $\tilde{\eta}$, more complex fiber shapes were observed (**Figure 3*a***, subpanel *ii*), corresponding to the eigenshapes predicted by the linear stability analysis. Fiber trajectories from experiments and simulations (**Figure 3*b***) show fiber transport across the cellular array. Due to the complexity of the flow, buckling does not take place at each passage of a stagnation point but depends on the exact conformation and position of the approaching fiber (Quennouz et al. 2015).

The relaxation of buckled fibers in a quiescent fluid has been investigated (Prasath et al. 2016). These experiments confirmed that the relaxation dynamics are governed by the timescale for elastic relaxation, $\tilde{\eta}/\dot{\gamma}$.

Buckling instabilities have also been investigated in the presence of Brownian fluctuations. Manikantan & Saintillan (2015) have shown numerically that Brownian fluctuations play a minor role in the buckling instability and serve mainly to broaden the threshold of the transitions toward the different buckling modes. Kantsler & Goldstein (2012) investigated the deformation of a micrometric actin fiber held at a stagnation point created in a microfluidic cross-slot device. Their experiments, as well as numerical simulations by Manikantan & Saintillan (2015), showed modes qualitatively similar to the deterministic predictions, albeit with shape fluctuations owing to Brownian fluctuations (see **Figure 3*c*,*d***).

The optimal flow geometry for the investigation of buckling instabilities is a hyperbolic channel, where constant extension rates can be achieved over long residence times. This was realized recently using actin filaments transported in an optimized microfluidic flow geometry (Section 2.2), and preliminary results can be seen in **Figure 3*e***. The filament is first stretched in the converging part of the channel where Brownian fluctuations are suppressed by the viscous forces. Then the filament enters the diverging part of the channel, where it experiences strong compression, leading to higher buckling modes. A similar succession of stretching and coiling has been observed experimentally in microchannels with constrictions for actin filaments (Strelnikova et al. 2017) and polymeric microfibers (Nunes et al. 2012) and has been investigated numerically using mesoscale hydrodynamics simulations (Chelakkot et al. 2012).

4.1.2. Fiber morphology in shear flows. A linear shear flow is the superimposition of a rotational and a straining flow, and as a consequence, fiber dynamics is a combination of tumbling and periodic deformation. A rigid ellipsoid tumbles periodically in a linear shear flow, while resisting stretching or compression as it rotates through the extensive and compressive quadrants. A flexible fiber, on the other hand, will react to the straining flow, leading to a transition to a buckling instability as $\tilde{\eta}$ increases (Forgacs & Mason 1959a, Becker & Shelley 2001, Liu et al. 2018). When $\tilde{\eta}$ increases further, fibers become too flexible to sustain rotation of the fiber as a whole, and a transition to snaking motion is observed. Here, the fiber remains mainly aligned with the flow direction but performs a tank-treading motion (Forgacs & Mason 1959b, Harasim et al. 2013, Nguyen & Fauci 2014, Delmotte et al. 2015, Liu et al. 2018).

Early experiments by Forgacs & Mason (1959b) investigated the deformation of millimetric elastic fibers in corn syrup under linear shear in a Couette cell. They were the first to address fiber buckling (Forgacs & Mason 1959a) and observed what they called springy rotations (Forgacs & Mason 1959b). For longer fibers, they identified snake turns, as shown in **Figure 4*a***. The transition to fiber buckling was clearly identified only later in a numerical investigation by Becker & Shelley (2001) for a fiber rotating in a linear shear flow. The first transition to buckling took place at $\tilde{\eta} = 306.4$. This was twice the value of $\tilde{\eta}_1 = 153.2$ found for straining flow, as the magnitude

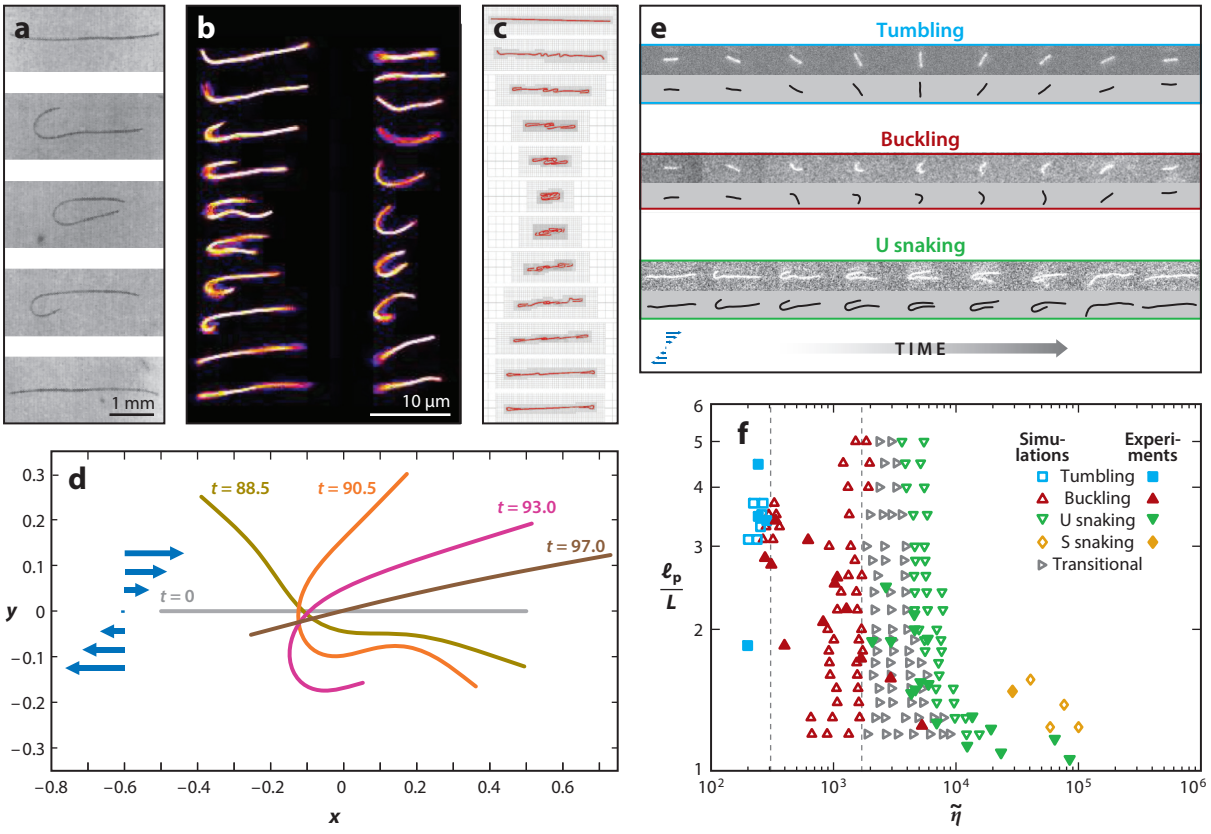

Figure 4

Fibers in shear flows. (*a*) Elastomeric fibers performing snake turns in corn syrup in a Couette cell. (*b*) Actin filaments in a microfluidic channel. (*c*) Complex fiber shapes from simulations using an adaptive version of the immersed boundary method. (*d*) Dynamics of a buckling fiber at $\tilde{\eta} = 7{,}000$ from simulations using local slender body theory (SBT). (*e*) Different morphologies of Brownian fibers with increasing length from experiments using actin filaments (*top*) and simulations using SBT (*bottom*). (*f*) Phase diagram of filament morphologies. The vertical lines indicate the transitions to buckling and snaking motions. Panels adapted with permission from (*a*) Forgacs & Mason (1959b), (*b*) Harasim et al. (2013), (*c*) Nguyen & Fauci (2014), (*d*) Becker & Shelley (2001), and (*e*,*f*) Liu et al. (2018).

of the straining part in shear flow is proportional to only half of the magnitude of the shear flow. The two threshold values are thus effectively identical. Using the local SBT formulation, their numerical simulations studied the very nonlinear shape dynamics of the fiber above the buckling transition (see **Figure 4*d***). Experiments by Harasim et al. (2013) using actin filaments in microscopic channel flows have investigated the snake turn motions in detail; they were the first to describe and model this configuration as a tank-treading motion, where a narrow bend travels along the filament whose two ends remain mainly aligned with the flow. They also addressed the role of rotational diffusion on the period of Jeffery orbits. Numerous investigations have observed the snaking dynamics numerically (see **Figure 4*c***) (Stockie & Green 1998, Nguyen & Fauci 2014, Delmotte et al. 2015). Only recently have experiments using actin filaments and a numerical investigation using nonlocal SBT in the presence of Brownian fluctuations (Liu et al. 2018) observed all subsequent regimes (**Figure 4*e***) and classified them as a function of $\tilde{\eta}$ and ℓ_p/L (**Figure 4*f***). Special care was taken when designing the experimental flow geometry to assure linear shear conditions (Section 2.2). The authors also addressed the transition to the snaking

mode, which is initiated by a buckling instability occurring, under sufficiently strong shear, in a filament that has not yet aligned with the compressive axis. Rotation of the deformed fiber will then align one end with the flow direction while the other can bend. The theoretically predicted threshold is in good agreement with experimental observations (**Figure 4*f***). The authors also reported more complex dynamics such as coiling (Nguyen & Fauci 2014), knot formation (Kuei et al. 2015), or helical motion (Forgacs & Mason 1959b) well above the onset of the snaking motion.

4.2. Fiber Morphology and Transport in More Complex Flows

Here we discuss the shape dynamics of fibers in more complex background flows, such as those arising from confinement or imposition of a background flow through external forcing.

4.2.1. Poiseuille flow and the interaction with bounding walls. Channel (or Poiseuille) flows represent the majority of experimental systems and, unlike linear shear flows, exhibit a shear gradient across the channel width. This can affect fiber morphology when fiber lengths are comparable to the channel dimensions. A first consequence is that buckling instabilities (as described above) are not observed and bending modes dominate. Typical fiber morphologies in Poiseuille flows are reminiscent of snaking motions (**Figure 4*b***) (Harasim et al. 2013) and can vary depending on the exact positioning within the flow (**Figure 5*a*,*b***) (Chelakkot et al. 2010, Reddig & Stark 2011). Secondly, several groups have demonstrated using bead numerical models (Chelakkot et al. 2010, Reddig & Stark 2011) or experiments with actin filaments (**Figure 5*c***) (Steinhauser et al. 2012) that semiflexible polymers show strong cross-stream migration in shear gradients and accumulate at preferred distances from channel walls. Similar predictions have been made for flexible fibers (Słowicka et al. 2013). Recently Nakielski et al. (2015) observed cross-stream migration using Brownian electrospun hydrogel nanofilaments in an oscillatory flow (**Figure 5*d***) and highlighted the dependance of migration dynamics on the initial fiber positioning.

4.2.2. Confined flows. Fiber transport in Hele–Shaw cells (**Figure 2*c***) represents a very different situation. Fibers with a diameter comparable to the cell height are confined by the top and bottom walls and evolve in two dimensions in a plug flow. Such confined microfabricated fibers (Section 2.1) have been observed to bend into a C-shape facing backward relative to the flow direction (**Figure 5*g***). At first sight, it is surprising that a fiber transported at zero force in a plug flow deforms, but this can be explained as follows: Friction with the top and bottom walls decreases the fiber velocity compared to the average flow velocity, and the fiber can be seen as a moving obstacle. The fiber thus creates a flow perturbation inducing an inhomogeneous force distribution along the fiber. Cappello et al. (2018) evaluated the force distribution as a function of fiber confinement using modified Brinkman equations. The resulting fiber shapes were found to be in good agreement with experimental findings. The coupling between fiber deformation, drift, and interaction with the side walls (Nagel et al. 2018) leads to complex trajectories and finally a preferred alignment with the flow direction (**Figure 5*g***).

4.2.3. Cellular flows. From their numerical study of fiber–flow interactions, Young & Shelley (2007) predicted that flexible fibers could move as random walkers across a closed streamline cellular flow (**Figure 5*h***). Occurring close to the stagnation points, fiber buckling yields an effective randomness due to its many degrees of freedom, allowing the fiber to cross streamlines and be transported across the flow. The precise transport properties depend in a nontrivial way on the fiber's flexibility and length, as has also been shown in experiments (Wandersman et al. 2010).

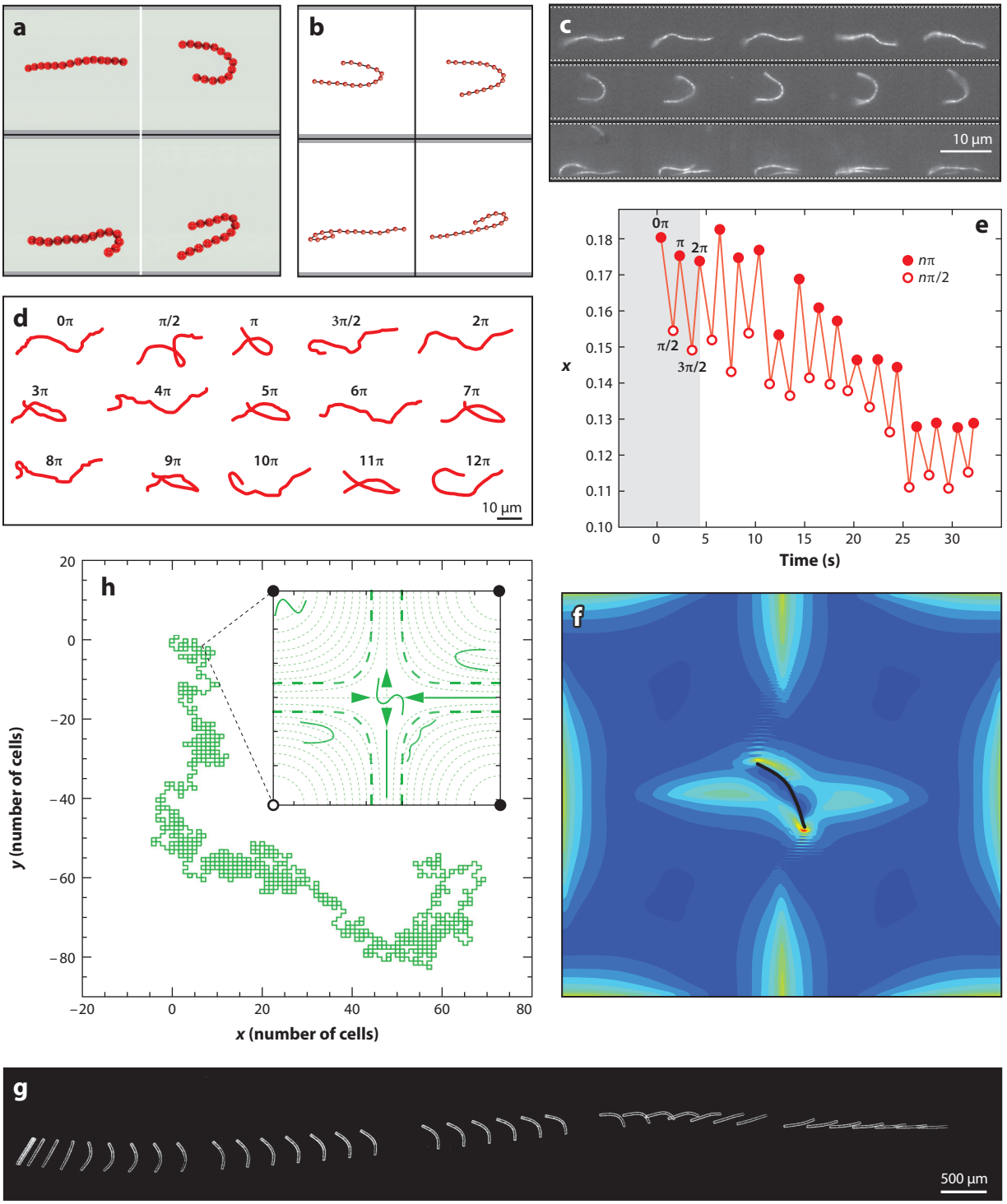

(Caption appears on following page)

Figure 5 (*Figure appears on preceding page*)

Fibers in complex flows. (*a–c*) Fiber shapes in Poiseuille flow from (*a*,*b*) bead–spring models and (*c*) experiments using actin filaments. Channel walls are represented by the black (*a*,*b*) or white dashed (*c*) horizontal lines. (*d*,*e*) An electrospun filament in an oscillatory flow, showing (*d*) different morphologies and (*e*) normalized filament–wall distance during successive oscillations. (*f*) A simulation of a flexible fiber in cellular flow of a non-Newtonian fluid. The color scale indicates polymer stretching. (*g*) The trajectory of a flexible polymeric fiber confined by the top and bottom walls of a microchannel. (*h*) The random walk of a flexible filament across a cellular flow (simulation). Panels adapted with permission from (*a*) Chelakkot et al. (2010), (*b*) Reddig & Stark (2011), (*c*) Steinhauser et al. (2012), (*d*,*e*) Pawłowska et al. (2017), (*f*) Yang & Fauci (2017), (*g*) Cappello et al. (2018), and (*h*) Young & Shelley (2007).

Numerical simulations by Manikantan & Saintillan (2013) addressed the role of Brownian fluctuations, which were shown to increase the trapping of filaments in vortices and thus decrease transport across the vortex array. Deng et al. (2015) have numerically confirmed these findings. Readers are referred to Bouzarth et al. (2011) and Young (2009) for numerical studies of two fibers interacting in such cellular flows and Yang & Fauci (2017) for transport in a polymeric cellular flow (**Figure 5*f***.)

5. SINGLE FIBERS MOVING UNDER EXTERNAL FORCES AND CONSTRAINTS

5.1. Sedimenting Fibers

When flexible fibers are subject to external forces such as gravity, the coupling between the elastic and viscous forces can induce a complex deformation and reorientation that strongly affects their macroscopic transport. Sedimentation is the classical example (although centrifugation would have similar consequences). Xu & Nadim (1994) first studied the sedimentation of flexible fibers from the theoretical point of view. Numerical studies have since been conducted using bead models (Cosentino Lagomarsino et al. 2005, Schlagberger & Netz 2005, Delmotte et al. 2015, Saggiorato et al. 2015) or SBT (Li et al. 2013). Only very recently have experimental studies been performed (Marchetti et al. 2018; V. Raspa, B. Marchetti, O. du Roure, A. Lindner & L. Bergougnoux, manuscript in preparation).

During sedimentation, fiber weight and viscous drag balance, and a rigid fiber settles at constant velocity and orientation. HIs along the fiber yield a viscous drag that is smaller in the middle than at the edges. For a flexible fiber, this inhomogeneous drag deforms the fiber and leads to rotation. The theoretical work of Li et al. (2013) first explored how this affects settling trajectories. As the drag depends on fiber orientation, the rotation leads to a nontrivial coupling between horizontal and vertical translations (**Figure 6*a***). This occurs until the fiber has reached an equilibrium configuration characterized by a constant settling velocity and a bent shape, the middle being perpendicular to gravity independently of the release conditions (**Figure 6*b***). Saggiorato et al. (2015) have explored numerically the behavior of very flexible and very heavy filaments whose shape can become nonplanar, resulting in drift or helical trajectories (**Figure 6*c***).

The fiber shape at equilibrium depends on the relative magnitudes of the gravitational force and the elastic restoring force. The relevant control parameter is $B = F_g L^2/E$, where F_g is the gravitational force (**Figure 6*d***) (Cosentino Lagomarsino et al. 2005, Delmotte et al. 2015, Saggiorato et al. 2015, Marchetti et al. 2018). For small B, the steady velocity is close to the horizontal settling velocity of a rigid fiber, while for large B, the fiber experiences large deformations and the velocity is close to the vertical settling velocity of a rigid fiber (**Figure 6*e***) (Delmotte et al. 2015). Marchetti et al. (2018) recently confirmed this experimentally and identified the intermediate regime as one of continuous drag reduction through fiber reconfiguration. Defining an elastoviscous number $\tilde{\eta}$ is not straightforward for this problem, as the viscous forces are functions of the fiber shape.

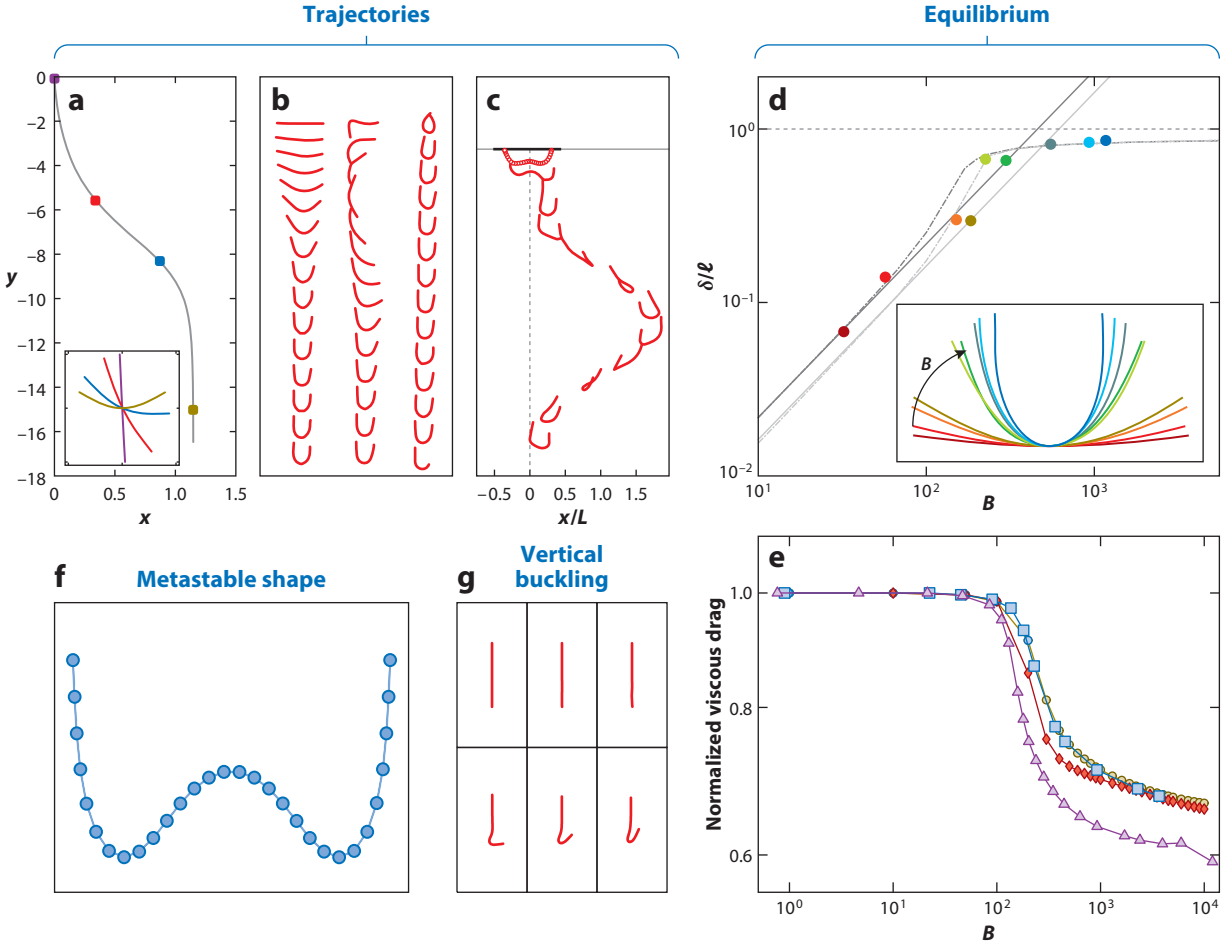

Figure 6

Sedimentation of flexible fibers. (*a*) The trajectory of the center of mass and the evolution of the shape (*inset*) for a sedimenting fiber. (*b*) The evolution of a sedimenting fiber from different initial conditions. (*c*) The complex behavior of a more flexible fiber. Panels *a*,*c* show numerical simulations and panel *b* shows experiments. (*d*) The maximal deformation of the fiber occurring at steady state, as a function of $B = F_g L^2/E$, where F_g is the gravitational force. Colored dots are from experiments, and gray lines are from theory or numerical simulations. (*Inset*) Filament shapes at steady state using the color code of the main graph. (*e*) Viscous drag at steady state as a function of B. (*f*) An example of a metastable configuration from a bead–spring model. (*g*) Buckling instability of the leading fiber half from simulations using slender body theory. Panels adapted with permission from (*a*) Li et al. (2013), (*b*,*d*) Marchetti et al. (2018), (*c*) Saggiorato et al. (2015), (*e*) Delmotte et al. (2015), (*f*) Cosentino Lagomarsino et al. (2005), and (*g*) Li et al. (2013).

The case of a fiber settling while aligned with gravity is very different: An inhomogeneous fiber tension results from the inhomogeneous viscous drag and is compressive in the leading half and extensile in the trailing part (Li et al. 2013). Above a certain threshold of the control parameter, buckling may occur in the leading half (**Figure 6*g***).

5.2. Anchored Fibers

Passive anchored fibers, such as the primary cilium (Young et al. 2012), are found in biological systems and can also form spontaneously under flow conditions as in the formation of biofilm

streamers (Drescher et al. 2013). In engineered microfluidic flow geometries, fabricated anchored fibers can be used as flow sensors, or conversely, the microfluidic flows can be used to measure the bending properties of unknown materials. Depending on the anchoring and flow orientation, either buckling or bending can occur.

5.2.1. Fiber buckling. Using local SBT, Guglielmini et al. (2012) investigated the stability of elastic fibers when held against an impinging linear or quadratic stagnation point flow (**Figure 7*a***). One fiber end is either clamped or hinged at the wall (i.e., free to rotate with zero applied torque). To identify critical values of $\tilde{\eta}$ for buckling transitions, they discretized the linearized dynamic equations and its boundary conditions and reposed the resulting finite-dimensional system as a generalized finite-dimensional eigenvalue problem for growth rates. For the clamped filament,

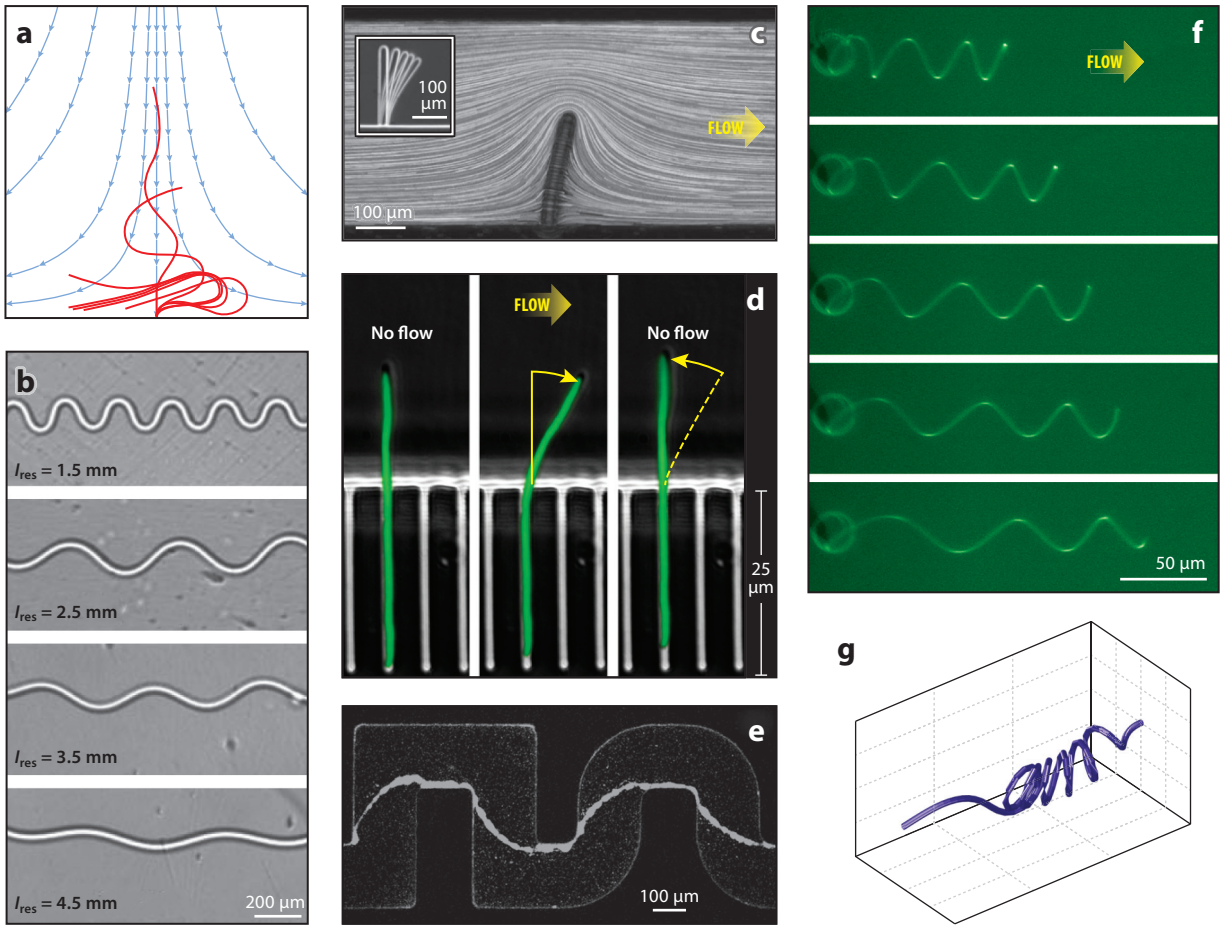

Figure 7

The deformation of anchored fibers. (*a*) The time evolution of a clamped filament buckling in an impinging flow (from simulations). (*b*) Buckling instability of a microfiber in a microchannel. (*c*,*d*) The deformation of objects anchored perpendicular to the flow, including (*c*) a photopolymerized fiber confined by top and bottom walls and (*d*) single-cell *Escherichia coli* grown in a lateral slit. (*e*) Biofilm streamers grown in a curved microchannel. (*f*) A micro-helix deformed by a flow. (*g*) A clamped microtubule growing against a wall (from simulations). Panels adapted from or provided by (*a*) Guglielmini et al. (2012), (*b*) Nunes et al. (2013), (*c*) Wexler et al. (2013), (*d*) Amir et al. (2014), (*e*) Rusconi et al. (2010), (*f*) Pham et al. (2015), and (*g*) E. Nazockdast. All panels reprinted with permission.

a first unstable bending mode was identified for both flow fields. The next unstable mode (in $\tilde{\eta}$) corresponds to buckling (**Figure 7*a***), with slightly different thresholds for the two flows. The hinged fiber is always unstable to rotation around its base, and its higher modes correspond to buckling, having significantly lower thresholds than free fibers.

Experimental studies of fiber buckling in impinging flows are difficult, as even a slight misalignment between the fiber base and the stagnation point leads to fiber bending (or rotation) instead of buckling. However, in situations where long fibers either remain temporarily pinned, as observed for fibers flowing in rough fractures (D'Angelo et al. 2009), or experience a compressive flow only locally, as observed during continuous fiber fabrication in a widening microfluidic device (Nunes et al. 2013), they show buckling instabilities similar to those of anchored fibers. In particular, Nunes et al. (2013) showed that such buckling can be used to form crimped microfibers with a well-defined morphology (**Figure 7*b***).

5.2.2. Fiber bending. The deformation of anchored fibers by viscous flows is akin in several simple flow geometries to a bending beam, where viscous forces play the role of a gravitational load. Microscopic beam bending has been used by Duprat et al. (2015) to determine the bending modulus of an elastomeric fiber fabricated using the ultraviolet projection method introduced in Section 2.1. Here, the fiber was confined between the top and bottom channel walls and held on both ends in a straight microchannel (**Figure 1*l***). In this configuration, flow takes place through the small gap above and below the fiber, and the viscous force applied can be determined using a simple lubrication analysis.

The flow geometry is more complex when a confined fiber is attached to one wall and so partially blocks a confined channel. The resulting flow profile has been visualized (**Figure 7*c***) in an experiment by Wexler et al. (2013) using fibers attached to the wall of a microchannel and perpendicular to the flow direction. A theoretical model (Wexler et al. 2013) provided insight into the competition between bending and leakage flow, showing good agreement with their experimental results, and was also used to measure fiber rigidity. By knowing its mechanical properties, such a fiber could be used as a flow sensor in microfluidic devices.

Amir et al. (2014) studied the flow-induced bending of single-cell *Escherichia coli* growing from slits in the side walls of a microfluidic channel (**Figure 7*d***). By applying a flow perpendicularly to the cells in their unconfined flow geometry, the experimental setup corresponds again to a simple bending beam experiment, where the force applied to the cell results from the viscous friction of the fluid. By estimating this viscous force and using linear elasticity theory, the authors were able to estimate the bending stiffness of the *E. coli* cells from the measured deflection. The simple hydrodynamic setup gave values similar to those obtained using much more costly techniques such as atomic force microscopy measurements.

Another biological example is the primary cilium. The primary cilium is a nonmotile and flexible hair-like protrusion from a cell into the extracellular space and is found in a variety of vertebrate cells. The primary cilium is believed to act as a mechanoreceptor by bending in response to flow, as is observed in kidney tubule cells. Young et al. (2012) have investigated its dynamics in a combined experimental and theoretical study.

More complex flow geometries are experienced by biofilm streamers that grow into long, filamentous elastic structures under flow (Rusconi et al. 2010, 2011). Autrusson et al. (2011) numerically determined the shape of elastic fibers within flows with curved streamlines for fibers anchored, either hinged or clamped, at given positions near a 2D corner. This work shows that, due to tension and bending forces within the fibers, the fibers do not align with the flow but rather cross flow streamlines. This is in agreement with Rusconi et al.'s (2010, 2011) experimental observations, shown in **Figure 7*e***.

5.2.3. Stretching of helical fibers. Pham et al. (2015) studied the stretching of very flexible anchored microhelices by flow. Here, the viscous drag represents a distributed loading, leading to a nonuniform pitch distribution (**Figure 7*f***). The overall helix extension is well described by the finitely extensible nonlinear elastic spring model, with the linear part simply given by the ratio of viscous to bending forces. The microscale helical ribbons with nanoscale thickness serve both as model systems for bacterial flagellae and as very sensitive flow sensors.

5.3. Actuated Fibers

Biological cilia and flagellae are of central importance to biophysical processes like propulsion or embryogenesis (Bray 2001, Hirokawa et al. 2006, Babu & Roy 2013). Both are elongated fibers anchored to cellular membranes that beat or rotate via the action of internal molecular motors [like the cilia covering the surface of microorganisms; see Camalet et al. (1999)] or rotating motors anchored at their base [like bacterial flagellae; see Bray (2001)]. Their interactions with the surrounding fluid medium, and the subsequent shape deformations, lead to useful transport processes like propulsion or mucus clearance in the lung. The study of anchored filaments submitted to forces is also very important for understanding the coupling between cytoskeletal filaments and molecular motors that occurs in the cell during intracellular trafficking (e.g., Trong et al. 2015, Shelley 2016), as well as for designing microrobots capable of motion in a fluid.

In the large literature on this topic that is largely beyond the scope of this review, fibers are usually anchored to a wall, but in some studies, fibers are attached to an object small enough to be moved by the fiber motions (i.e., flagellae and bacteria). This was studied at the micron-scale in two different experiments (**Figure 8*a*,*b***). Early to the field, Wiggins et al. (1998) attached an actin filament to a bead that was periodically driven by an optical trap. The bead oscillations induced traveling waves on the fiber that generated a propulsive force. In another realization of this phenomenon, Dreyfus et al. (2005) built an artificial microswimmer from a chain of magnetic

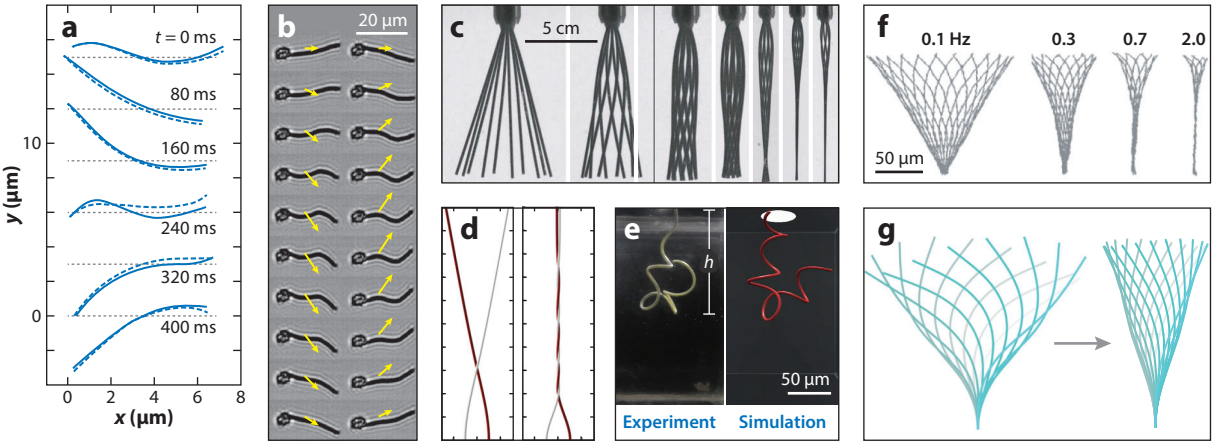

Figure 8

Anchored and driven fibers. (*a*) Deformation of a microscopic fiber attached to a bead moved vertically by an optical trap. (*b*) A magnetically actuated fiber propelling a red blood cell. (*c*) The rotation of a tilted elastic filament in a viscous bath at increasing rotation velocity. (*d*) The attractive interaction between two elastic fibers rotating around their own axes. (*e*) The buckling of a rotating flexible helix. (*f*,*g*) Shapes of beating fibers, showing (*f*) a magnetic fiber beating in a plane and (*g*) a simulation of a fiber actuated at its free end by a follower force aligned with the fiber. Panels adapted with permission from (*a*) Wiggins et al. (1998), (*b*) Dreyfus et al. (2005), (*c*) Coq et al. (2008), (*d*) Man et al. (2017), (*e*) Jawed et al. (2015), (*f*) Babataheri et al. (2011), and (*g*) De Canio et al. (2017).

beads attached to a red blood cell—only to break symmetry—and actuated the chain with a time-dependent magnetic field.

In another class of studies, fiber motion is induced by the rotation of the anchoring point. Wolgemuth et al. (2000) took inspiration from biology to model the deformations induced by the rotation of a fiber around its axis in a viscous fluid. Rotation, twisting, and bending combine to yield different regimes of rotation, with one of them having the free end repelled from the axis. Man et al. (2017) recently studied numerically and experimentally the interaction of two rotating fibers (**Figure 8*d***) and showed that the induced rotational flows tend to bend the fibers around each other. If a fiber is tilted at the anchoring point relative to its rotation axis, the interaction with the fluid leads to the collapse of the fiber onto the rotation axis (**Figure 8*c***) while it assumes a helicoidal shape that generates a propulsive force (Manghi et al. 2006, Coq et al. 2008, Qian et al. 2008). The rotation of a flexible helix can result in a propulsive force sufficiently large to induce buckling (**Figure 8*e***) (Jawed et al. 2015). The flexibility and buckling of the flagellar hook at the base of the flagellum plays an important role in the swimming of mono-flagellated bacteria, where its buckling yields changes in the swimming direction (Son et al. 2013). Interactions between two weakly flexible helices result in bundling, as has been shown experimentally by Kim et al. (2003). As a model for cilia, Guo et al. (2018) studied the hydrodynamic coupling of immersed elastic fibers driven at their base by an applied torque. For two fibers, their simulations and theory showed that bistability of in-phase and out-of-phase oscillations can arise from a coupling of elasticity and drive to flow.

Forced fibers can be actuated either locally or all along the body. The latter case has been experimentally and numerically modeled by magnetic colloid chains (**Figure 8*b*,*f***) (Dreyfus et al. 2005, Gauger & Stark 2006, Babataheri et al. 2011). The former has been addressed in different experimental and numerical studies, mainly with the forcing being applied to the anchoring point as discussed above (Wiggins et al. 1998, Wolgemuth et al. 2000, Manghi et al. 2006, Coq et al. 2008, Qian et al. 2008, Guo et al. 2018). The associated dynamics is typically oscillatory. De Canio et al. (2017) recently studied tangential forcing at the fiber free end as a model for the action of motor proteins on microtubules and demonstrated a bifurcation to beating via a buckling instability (**Figure 8*g***). Their analysis and simulations were restricted to fiber motions in two dimensions. Ling et al. (2018) generalized this to consider loading by a distribution of axial forces and allowed for fully 3D dynamics. They showed the existence of bifurcations to both 2D beating states and 3D spinning states.

6. MICRO-MACRO COUPLING AND COLLECTIVE BEHAVIOR

We have thus far focused on single fibers (or a few fibers) interacting with flows. However, in most industrial and natural settings, flexible fibers are mostly found collectively and in suspension. Understanding the transport and rheology of fibrous suspensions at macroscopic length scales is of significant importance. In this section, we review studies on the relationship between microscopic dynamics of suspended fibers and macroscopic rheology, as well as situations where fibers act collectively in their interactions with flow, as in ciliary beds or in new flow control devices.

The main difficulty in studying fibrous assemblies or suspensions is the complex and long-ranged nature of HIs. The importance of fiber interactions is determined by their average separation distance. In the dilute regime, fibers' separation distance is much larger than their length, $nL^3 \ll 1$, where n is the fiber number density. In this limit, HIs can be neglected, and for a suspension, the ensemble behavior can be estimated from the dynamics of a single fiber interacting with the flow. Increasing the concentration causes HIs to be stronger. In the semidilute regime of $nL^3 \gtrsim 1$, the distance between fibers becomes less than their length, and both HIs and

possibly steric interactions become important. With further increase of concentration, the separation distance becomes comparable to the fiber radius, and rotational motions are hindered. For suspensions, this can result in the formation of liquid crystalline phases (Doi & Edwards 1978), which is beyond the scope of this review.

6.1. Rheology of Fiber Suspensions

Here we give a brief review of the studies on the rheology of semiflexible fiber suspensions.

6.1.1. Linear rheology of dilute non-Brownian suspensions. The analysis of rheology for non-Brownian suspensions in oscillatory background shear flows is very similar to the buckling instability analysis in simple flows in Section 4.1.1. For small perturbations of fiber shape from a straight rod whose dynamics is described by Equation 11, Equation 6 reduces to

$$\tilde{\eta}\,(w_t - w\cos\tilde{\omega}t) = -w_{ssss} + 2\bar{T}_s\,w_s + \bar{T}w_{ss} \quad \text{and} \quad \bar{T} = -\frac{\tilde{\eta}}{4}\left(s^2 - \frac{1}{4}\right)\cos\tilde{\omega}t, \qquad 13.$$

where w is the perturbation transverse to the fiber orientation in the plane of shear, and $\tilde{\omega}$ is the oscillation frequency normalized by the maximal shear rate $\dot{\gamma}$.

Perturbations will decay so long as $\tilde{\eta}$ is less than 306.4, the first bifurcation to buckling for the constant shear case. In that case, the long-time behavior will then be that of an oscillating rigid fiber that, because of time-reversibility, will yield only a viscous response under time averaging. For values of $\tilde{\eta}$ beyond the buckling transition, fibers under compressive stress will buckle and then be straightened out in the reverse part of the cycle. Since elasticity is relaxational throughout the oscillation, it remains unclear whether the long-time behavior supports persistent buckling. If not, the rheology will be purely viscous.

6.1.2. Linear rheology of dilute Brownian suspensions. The linear viscoelastic behavior of semiflexible polymers has been widely studied over the past two decades. Examples of these systems include worm-like polymers, cytoskeletal filaments, and nanotubes. A detailed discussion of the literature in this limit is beyond the scope of this review, and readers are referred to Shankar et al. (2002) and Morse (1998). Here we give a very brief summary relevant to this review.

Rotational diffusion is the slowest timescale for Brownian semiflexible polymers and is given by $\tau_{\rm rot} \sim \mu L^3/(k_{\rm B}Tc)$. Another timescale arises from curvature relaxation, given by $\tau_{\rm curv} = 8\pi\mu L^4/Ec$. The ratio of bending to rotational diffusion timescales is $\tau_{\rm curv}/\tau_{\rm rot} = L/\ell_{\rm p} \ll 1$. The fastest relaxation time is associated with tensile forces. In a rigid fiber, the tension is set instantaneously. The presence of thermal forces induces shape fluctuations in semiflexible polymers. Thus, the average end-to-end length of the polymer will be less than its full contour length and will change under external flows/forces. The tension timescale is roughly defined as the time $\tau_{\rm T}$ over which the end-to-end distance of the polymer reaches mechanical equilibrium under small external forces (Shankar et al. 2002). The tension dynamics is more involved but has been studied in depth (Morse 1998, Everaers et al. 1999, Pasquali et al. 2001). These studies found that $\tau_{\rm T}/\tau_{\rm curv} = (L/\ell_{\rm p})^4$ is significantly less than unity. Thus, we have $\tau_{\rm T} \ll \tau_{\rm curv} \ll \tau_{\rm rot}$. This separation of timescales and the linear response in small deformation allow for analytical solutions of Equation 9 in Section 3.3, which was outlined by Shankar et al. (2002).

Having calculated the shape of the fiber, the time-dependent particle stress tensor is found by the force moment integral along the fiber, $\mathbf{S} = \int_0^L \mathbf{X}(s)\mathbf{f}(s)\,ds$, recalling that $\mathbf{f} = \mathbf{f}^{\rm E} + \mathbf{f}^{\rm B}$ where $\mathbf{f}^{\rm E} = (T\mathbf{X}_s)_s - E\mathbf{X}_{ssss}$, and $\mathbf{f}^{\rm B}$ is given by Equation 10. In dilute suspensions, the interactions between the fibers are ignored, and the ensemble-average stress reduces to $\Sigma_{\rm F}(t) = n\langle\mathbf{S}\rangle$. Shankar et al. (2002) used this expression to compute elastic and loss moduli in oscillatory shear flow for different values of $L/\ell_{\rm p}$. **Figure 9*a*** gives a schematic presentation of the tensile, bending, and

thermal contributions to the time-dependent shear modulus relaxation in a step strain deformation (see figure 2 of Shankar et al. 2002). At very short times $t \ll \tau_{curv}$, the shear modulus and its relaxation time are determined by tensile forces, while for $t \sim \tau_{curv}$, all forces contribute equally to the rheology. Finally, at long times the behavior is dominated by thermal forces; thus, the long-time behavior is viscous.

6.1.3. Nonlinear shear rheology of dilute suspensions. Becker & Shelley (2001) used local SBT to simulate large-amplitude buckling of flexible fibers in shear flow (see **Figure 4*d***). They showed that fiber buckling gave rise to positive first normal stress differences and that the predicted threshold to buckling agreed well with the onset of positive first normal stress differences in shearing experiments of nylon fibers in glycerin (Goto et al. 1986).

Tornberg & Shelley (2004) confirmed this observation in their nonlocal SBT simulations. **Figure 9*a*** shows the numerical predictions of Tornberg & Shelley for the first normal stress difference induced by a single flexible fiber in shear flow, $N_1 = \mathbf{S}_{xx} - \mathbf{S}_{yy}$, during one rotation of the fiber. The results for a rigid rod are shown for comparison. To understand the physical basis for this behavior, it helps to study the fiber's shape in three instances: (*a*) the beginning of the deviation from a rigid rod, (*b*) when the deviations are maximized, and (*c*) the return to a rigid rod behavior. These instances are shown with their corresponding shapes in **Figure 9*a***. We see clearly that the deviation coincides with the buckling of fibers under compressional stress ($\mathbf{p} \cdot \mathbf{E} \cdot \mathbf{p} < 0$). As the fiber rotates to the extensional quadrant ($\mathbf{p} \cdot \mathbf{E} \cdot \mathbf{p} > 0$), it is stretched back by the straining component of the shear flow to its initial straight shape, and the corresponding stress approaches that of a rigid rod. Intuitively, buckling reduces the effective hydrodynamic length (the end-to-end distance) of the fiber, decreasing the stress magnitude in comparison with a rigid rod (recall that $|\mathbf{S}| \sim L^3$). Once the fiber moves to the extensional flow quadrant, it straightens and its effective length increase causes the stress magnitude to approach that of a rigid rod.

6.1.4. Shear rheology of semidilute suspensions. Several aspects of the rheology of flexible fibers in a semidilute regime remain poorly understood due to the complexity of long-range HIs. To our knowledge, there is no large-scale simulation of flexible fibers in shear flow, with the exception of that of Tornberg & Shelley (2004), who studied the suspension of $N_F = 25$ flexible fibers in oscillatory shear flow. They observed that at large-enough shear rates, the fibers deform during the period they are in compressional quadrants of the flow. The fibers are then stretched back once they move to the extensional quadrants. However, they do not entirely relax, perhaps because of fiber–fiber interactions, and maintain strong buckling into the ensuing periods. They also observed that the total stored elastic energy is a strong function of the initial configuration of the filaments, which the authors related to the small number of fibers in their simulations. For the same reason, they did not report on the rheology of the suspension. To our knowledge, there is currently no prediction of shear viscosity and normal stresses versus shear rate.

On the experimental front, Huber et al. (2014) studied the dynamics of individual actin filaments in semidilute solutions of mixtures of labeled and nonlabeled filaments flowing in microchannels. They showed that steric hindrance reduces the tumbling rate significantly in semidilute solutions as compared to isolated filaments. Entanglements between filaments can also lead to anomalous or aborted tumbling events. The authors linked the microscopic filament dynamics to the shear thinning viscosity of the semidilute solution via an effective diffusion coefficient.

The effect of entanglements on the 3D deformations of actin filaments in a semidilute solution was investigated experimentally by Kirchenbuechler et al. (2014). They used confocal microscopy on a cone-and-plate counterrotating shear cell and simultaneously observed microscopic filament dynamics and macroscopic flow properties (**Figure 9*b***). They showed that shear flow causes stretching and alignment of hairpin-shaped filaments, explaining the observed shear thinning.

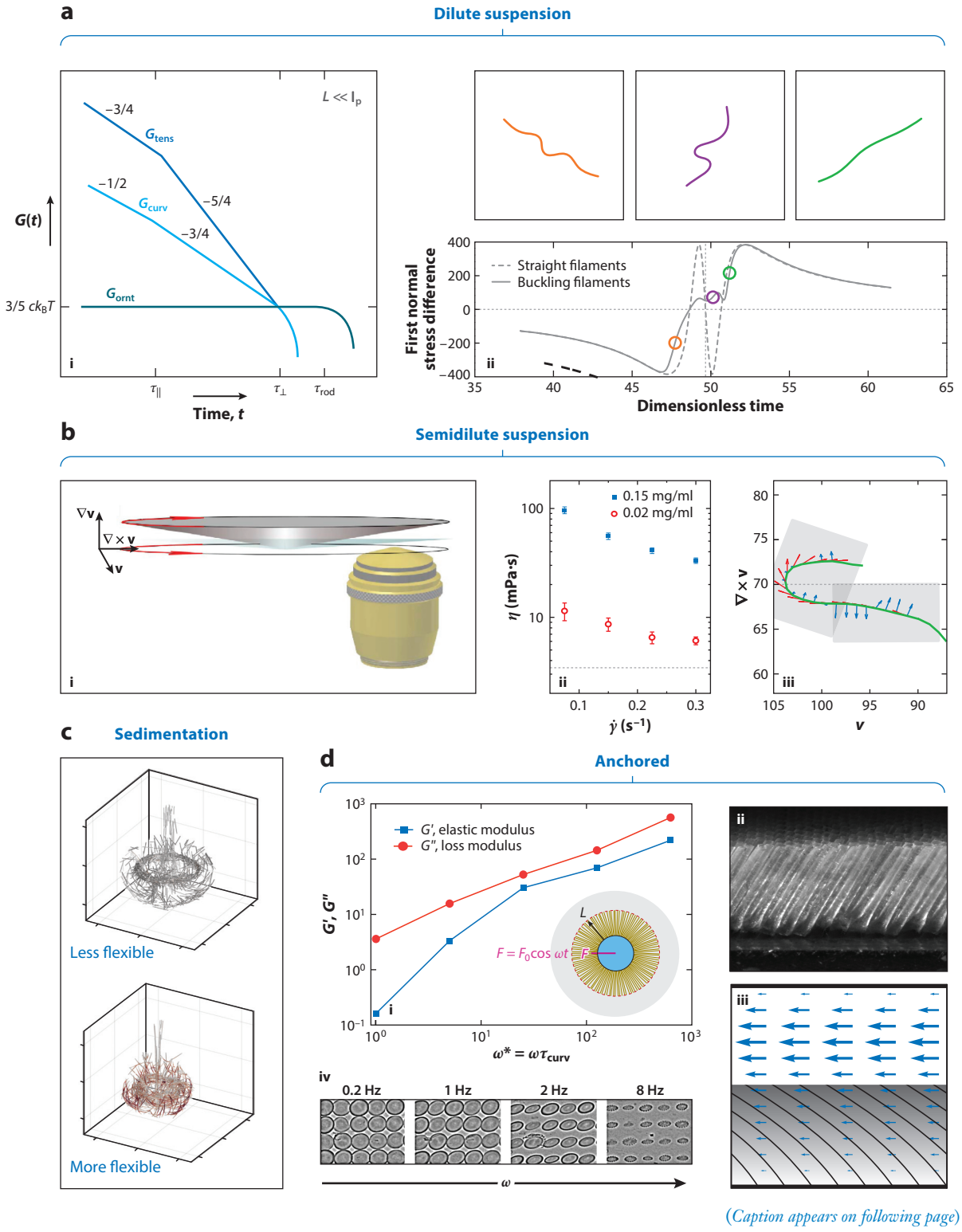

(*Caption appears on following page*)

Figure 9 (*Figure appears on preceding page*)

Collective behavior. (*a*) Dilute suspensions: (*i*) asymptotic contributions of tensile, bending, and thermal forces to the shear modulus $G(t)$ for semiflexible polymers, for $\tau_\perp \equiv \tau_{\text{curv}} = 8\pi\mu L^4/Ec$, $\tau_\parallel \equiv \tau_\text{T} = (L/\ell_\text{p})^4\tau_{\text{curv}}$, and $\tau_{\text{rod}} \equiv \tau_{\text{rot}} = \mu L^3/(k_\text{B}Tc)$, and (*ii*) the first normal stress difference during shear for straight filaments and buckling filaments, corresponding to the shapes on the top row. (*b*) Semidilute suspensions: (*i*) experimental setup combining rheometry and confocal microscopy for (*ii*) measuring shear viscosities η of an actin filament suspension as a function of shear rate $\dot{\gamma}$ and (*iii*) three-dimensional imaging of filament shapes. (*c*) Sedimentation: a torus ring formed during the sedimentation of a cloud of 1,024 flexible fibers. (*d*) Anchored fibers: (*i*) the rheology of a radially anchored flexible fiber shell, (*ii*) an array of tilted elastic fibers, (*iii*) a simulation of flow through an anchored bed of flexible fibers using a continuum model of an elastic fiber Brinkman medium, and (*iv*) a trajectory of the tips of many rotating magnetic fibers with increasing frequency. Panels adapted with permission from (*a*,*i*) Shankar et al. (2002); (*a*,*ii*) Tornberg & Shelley (2004); (*b*) Kirchenbuechler et al. (2014); (*c*) Nazockdast et al. (2017b); (*d*,*i*) Nazockdast et al. (2017b); (*d*,*ii*) Alvarado et al. (2017); (*d*,*iii*) D. Stein & M. Shelley, manuscript in preparation; and (*d*,*iv*) Coq et al. (2011).

A very different behavior was observed by Perazzo et al. (2017) for concentrated suspensions of very long fibers. Using a microfluidic fabrication method (**Figure 1*i***), they produced concentrated suspensions of fibers with an aspect ratio greater than 100 and showed that gelation, resulting from the formation of mechanical interlocking of chains, is triggered by flow. This is also a very simple way to produce biocompatible hydrogels.

6.2. Sedimentation of Fiber Assemblies

The sedimentation of particles in fluids has been a major area of research in suspension mechanics over the past several decades (Guazzelli & Hinch 2011). There have also been several experimental (Herzhaft & Guazzelli 1999, Metzger et al. 2005) and numerical (Butler & Shaqfeh 2002, Saintillan et al. 2005, Tornberg & Gustavsson 2006) studies on sedimentation of suspensions of rigid fibers. The complex behavior in sedimenting suspensions is due to HIs (Ramaswamy 2001, Butler & Snook 2018). For instance, sedimenting fiber suspensions form inhomogeneous clusters resulting in enhanced sedimentation rates of those clusters in both numerical and experimental studies (Metzger et al. 2005, Saintillan et al. 2005, Tornberg & Gustavsson 2006). Manikantan et al. (2014) studied the effect of fiber flexibility under small deformations on sedimentation using a continuum theory, later followed by particle simulations (Manikantan & Saintillan 2016). These studies showed that flexibility can have both a stabilizing (no clusters) and destabilizing (cluster formation) effect, depending on the relative magnitudes of fiber flexibility and rotational diffusion.

Another interesting problem is the sedimentation of particle clouds. Experiments and simulations have used rigid rods and spheres to show that an initially spherical cloud evolves into a descending toroidal shape reminiscent of a high–Reynolds number vortex ring. The torus eventually breaks into smaller clouds that evolve into tori (Machu et al. 2001; Metzger et al. 2005, 2007; Park et al. 2010). Nazockdast et al. (2017b) used nonlocal SBT to study clouds of $N_\text{F} = 1{,}024$ flexible fibers in a semidilute regime. Their observations were in general agreement with the previous experimental and computational studies on rigid rods (**Figure 9*c***). They observed no qualitative effect of fiber flexibility on the collective behavior of the cloud, although flexibility does result in changes in the shape of the torus ring (E.N. Nazockdast & M.J. Shelley, manuscript in preparation). **Figure 9*c*** shows the tori for two clouds with fibers of differing effective rigidities (a ratio of 65). In short, increasing flexibility results in smaller tori.

6.3. Collective Dynamics of Anchored Fibers

In many biological processes and industrial applications, fiber assemblies are attached to substrates and particles. Detailed theoretical descriptions are still few, and a full accounting is beyond the scope of our review, but we discuss several interesting recent examples.

Alvarado et al. (2017) have recently shown how to construct soft flow rectifiers by mounting dense beds of tilted flexible fibers onto the walls of a flow channel (**Figure 9*d***, subanel *ii*). When fluid is driven in the direction of the fiber tilt, the fiber bed depresses and facilitates flow. When fluid is pumped in the opposite direction, the bed rises and occludes flow. The mechanical responses were quantified in a Taylor–Couette device, and rationalized theoretically using a homogeneous Brinkman approximation for fluid flow through the bed.

In a related but very different work, Nazockdast et al. (2017b) studied the rheology of centrosomal arrays of flexible microtubules in eukaryotic cells. Using nonlocal SBT, they simulated the dynamics of flexible fibers radially anchored to a sphere moving under an external oscillatory force, $F = F_0 \cos \omega t$ (**Figure 9*d***, subpanel *i*). At low frequencies, the response was purely viscous, and the fiber array was well modeled as a homogeneous Brinkman medium. At higher frequencies, the force and velocity response moved out of phase, reflecting viscoelasticity, and they used the phase lag to approximate the elastic and loss moduli, G' and G'', respectively (**Figure 9*d***, subpanel *i*). For a single fiber, G''/G' has a minimum at $\omega_1 = \tau_{\text{curv}}^{-1}$. A minimum was also observed in the many-fiber simulation but at $\omega \approx 25\tau_{\text{curv}}^{-1}$. In other words, HIs between the fibers decreased the relaxation time by a factor of about 25.

Nazockdast et al. (2017a) used the same computational framework to study pronuclear positioning, an important transport process in eukaryotic cells. They showed that ignoring HIs leads to order-of-magnitude mispredictions of the necessary positioning forces. They also showed that different proposed models for the active forces give rise to different cellular flows, and they proposed flow measurement as a tool to differentiate between active mechanisms.

Beds of actively beating cilia are common in biology, propelling ciliated organisms, pumping fluid in the brain (Faubel et al. 2016), performing selective filtering (Nawroth et al. 2017), and clearing mucus from the lungs. Mitran (2007) carried out a 3D simulation of propagating metachronal waves in rows of pulmonary cilia. He considered a system where cilia sit primarily in a Newtonian viscous fluid, while the tips move within a viscoelastic fluid modeling a mucus layer. He found that minimizing the work done by molecular motors results in the synchronized beating of cilia and suggested that HIs between cilia can lead to synchronized beating. Ding et al. (2014) used a regularized Stokeslet method to study the dynamics of an infinite bed of driven cilia. They showed that metachronal waves not only enhance fluid transport above the bed but also increase the mixing of fluid within it. Finally, Coq et al. (2011) experimentally investigated the dynamics of extended arrays of artificial cilia driven by a precessing magnetic field. Whereas the dynamics of an isolated cilium was rigid body rotation, collective driven beating results in a symmetry breaking of the precession patterns. The trajectories of the cilia are anisotropic and experience a significant structural evolution as the actuation frequency increases (**Figure 9*d***, subpanel *iv*).

7. SUMMARY AND OUTLOOK

As should be clear, flexible fibers interacting with flowing liquids present a rich source of problems in fluid–structure interactions. They also present complicated phenomena, which require sophisticated experimental techniques to observe and measure, and complicated theories through which to understand them.

There are many areas of open inquiry, among them the interactions of fibers with complex media. Viscoelastic responses are typical of many biological environments, such as the reproductive tract (Fauci & Dillon 2006) or the interior of the cell (Wirtz 2009). There is a developing literature on swimming microorganisms in viscoelastic fluids (Elfring & Lauga 2015, Sznitman & Arratia 2015). Using a 2D slender body–actuated elastica model, Thomases & Guy (2017) recently studied the role of body flexibility for undulatory swimming in viscoelastic fluids. There have been few

if any studies of flexible fibers interacting with complex flows of complex fluids; Yang & Fauci's (2017) recent simulations of fiber transport by cellular viscoelastic flow (**Figure 5*f***) is the first of which we are aware. The fundamental theoretical difficulty is the necessity of evolving bulk elastic stresses via transport nonlinearities. This makes fluid–structure problems involving viscoelastic flows very challenging and at the level of difficulty of those for the Navier–Stokes equations. On the experimental side, it remains challenging to synthesize complex fluids with well-characterized (and simple!) rheological responses.

New kinds of mathematical coarse-grained descriptions need to be developed to describe the collective behavior of flexible fibers in fluids, especially when hydrodynamic interactions are strong. One regime where progress is being made is when the fibers can be considered well aligned. In recent work, D. Stein & M. Shelley (manuscript in preparation) have developed a continuum Brinkman-type model that captures the anisotropic drag from elongated flexible structures to compute the flow feedback to the bending and tensile response of a porous elastic medium (Moeendarbary et al. 2013, Strychalski et al. 2015). Subpanel *iii* of **Figure 9*d*** shows the model's result in simulating a soft flow rectifier by the bending of a bed of tilted and anchored elastic fibers shown in subpanel *ii*.

DISCLOSURE STATEMENT

The authors are not aware of any biases that might be perceived as affecting the objectivity of this review.

ACKNOWLEDGMENTS

E.N.N. and M.J.S. acknowledge the support of the National Science Foundation, the National Institutes of Health, and the Department of Energy. A.L. acknowledges support from European Research Council Consolidator Grant 682367 under the European Union's Horizon 2020 program.

LITERATURE CITED

Alvarado J, Comtet J, De Langre E, Hosoi AE. 2017. Nonlinear flow response of soft hair beds. *Nat. Phys.* 13:1014–19

Amir A, Babaeipour F, McIntosh DB, Nelson DR, Jun S. 2014. Bending forces plastically deform growing bacterial cell walls. *PNAS* 111:5778–83

Attia R, Pregibon DC, Doyle PS, Viovy JL, Bartolo D. 2009. Soft microflow sensors. *Lab Chip* 9:1213–18

Autrusson N, Guglielmini L, Lecuyer S, Rusconi R, Stone HA. 2011. The shape of an elastic filament in a two-dimensional corner flow. *Phys. Fluids* 23:063602

Babataheri A, Roper ML, Fermigier M, du Roure O. 2011. Tethered fleximags as artificial cilia. *J. Fluid Mech.* 678:5–13

Babu D, Roy S. 2013. Left–right asymmetry: Cilia stir up new surprises in the node. *Open Biol.* 3:130052

Becker L, Shelley M. 2001. The instability of elastic filaments in shear flow yields first normal stress differences. *Phys. Rev. Lett.* 87:198301

Berthet H, du Roure O, Lindner A. 2016. Microfluidic fabrication solutions for tailor-designed fiber suspensions. *Appl. Sci.* 6:385

Bouzarth E, Layton A, Young YN. 2011. Modeling a semi-flexible filament in cellular Stokes flow using regularized Stokeslets. *Int. J. Num. Meth. Biomed. Eng.* 27:2021–34

Bray D. 2001. *Cell Movements: From Molecules to Motility*. New York: Garland Sci.

Broedersz CP, MacKintosh FC. 2014. Modeling semiflexible polymer networks. *Rev. Mod. Phys.* 86:995–1036

Butler JE, Shaqfeh ES. 2002. Dynamic simulations of the inhomogeneous sedimentation of rigid fibres. *J. Fluid Mech.* 468:205–37

Butler JE, Snook B. 2018. Microstructural dynamics and rheology of suspensions of rigid fibers. *Annu. Rev. Fluid Mech.* 50:299–318

Camalet S, Jülicher F, Prost J. 1999. Self-organized beating and swimming of internally driven filaments. *Phys. Rev. Lett.* 82:1590–93

Cappello J, Duprat C, du Roure O, Nagel M, Bechert M, et al. 2018. Transport of flexible fibers in confined micro-channels. arXiv:1807.05158 [physics.flu-dyn]

Chelakkot R, Winkler RG, Gompper G. 2010. Migration of semiflexible polymers in microcapillary flow. *Europhys. Lett.* 91:14001

Chelakkot R, Winkler RG, Gompper G. 2012. Flow-induced helical coiling of semiflexible polymers in structured microchannels. *Phys. Rev. Lett.* 109:178101

Choi CH, Yi H, Hwang S, Weitz DA, Lee CS. 2011. Microfluidic fabrication of complex-shaped microfibers by liquid template-aided multiphase microflow. *Lab Chip* 11:1477–83

Coq N, Bricard A, Delapierre FD, Malaquin L, du Roure O, et al. 2011. Collective beating of artificial microcilia. *Phys. Rev. Lett.* 107:014501

Coq N, du Roure O, Marthelot J, Bartolo D, Fermigier M. 2008. Rotational dynamics of a soft filament: wrapping transition and propulsive forces. *Phys. Fluids* 20:051703

Cortez R. 2001. The method of regularized Stokeslets. *SIAM J. Sci. Comput.* 23:1204–25

Cortez R, Nicholas M. 2012. Slender body theory for stokes flows with regularized forces. *Commun. Appl. Math. Comput. Sci.* 7:33–62

Cosentino Lagomarsino M, Pagonabarraga I, Lowe CP. 2005. Hydrodynamic induced deformation and orientation of a microscopic elastic filament. *Phys. Rev. Lett.* 94:148104

D'Angelo MV, Semin B, Picard G, Poitzsch ME, Hulin JP, Auradou H. 2009. Single fiber transport in a fracture slit: influence of the wall roughness and of the fiber flexibility. *Trans. Porous Med.* 84:389–408

Darnige T, Bohec P, Lindner A, Clément E. 2017. Lagrangian 3D tracking of fluorescent microscopic objects in motion. *Rev. Sci. Instrum.* 88:055106

De Canio G, Lauga E, Goldstein RE, Goldstein RE. 2017. Spontaneous oscillations of elastic filaments induced by molecular motors. *J. R. Soc. Interface* 14:20170491

Delmotte B, Climent E, Plouraboué F. 2015. A general formulation of Bead Models applied to flexible fibers and active filaments at low Reynolds number. *J. Comput. Phys.* 286:14–37

Deng M, Grinberg L, Caswell B, Karniadakis GE. 2015. Effects of thermal noise on the transitional dynamics of an inextensible elastic filament in stagnation flow. *Soft Matter* 11:4962–72

Ding Y, Nawroth J, McFall-Ngai M, Kanso E. 2014. Mixing and transport by ciliary carpets: a numerical study. *J. Fluid Mech.* 743:124–40

Doi M, Edwards S. 1978. Dynamics of rod-like macromolecules in concentrated solution. Part 1. *J. Chem. Soc., Faraday Trans. 2* 74:560–70

Drescher K, Shen Y, Bassler BL, Stone HA. 2013. Biofilm streamers cause catastrophic disruption of flow with consequences for environmental and medical systems. *PNAS* 110:4345–50

Dreyfus R, Baudry J, Roper ML, Fermigier M, Stone HA, Bibette J. 2005. Microscopic artificial swimmers. *Nature* 437:862–65

Duprat C, Berthet H, Wexler JS, du Roure O, Lindner A. 2015. Microfluidic in situ mechanical testing of photopolymerized gels. *Lab Chip* 15:244–52

Elfring GJ, Lauga E. 2015. Theory of locomotion through complex fluids. In *Complex Fluids in Biological Systems*, ed. S Spagnolie, pp. 283–317. New York: Springer-Verlag

Everaers R, Jülicher F, Ajdari A, Maggs A. 1999. Dynamic fluctuations of semiflexible filaments. *Phys. Rev. Lett.* 82:3717

Faubel R, Westendorf C, Bodenschatz E, Eichele G. 2016. Cilia-based flow network in the brain ventricles. *Science* 353:176–78

Fauci LJ, Dillon R. 2006. Biofluidmechanics of reproduction. *Annu. Rev. Fluid Mech.* 38:371–94

Fiore AM, Balboa Usabiaga F, Donev A, Swan JW. 2017. Rapid sampling of stochastic displacements in Brownian dynamics simulations. *J. Chem. Phys.* 146:124116

Fixman M. 1978. Simulation of polymer dynamics. I. General theory. *J. Chem. Phys.* 69:1527–37
Flores H, Lobaton E, Méndez-Diez S, Tlupova S, Cortez R. 2005. A study of bacterial flagellar bundling. *Bull. Math. Bio.* 67:137–68
Forgacs OL, Mason SG. 1959a. Particle motions in sheared suspensions: IX. Spin and deformation of threadlike particles. *J. Colloid Sci.* 14:457–72
Forgacs OL, Mason SG. 1959b. Particle motions in sheared suspensions: X. Orbits of flexible threadlike particles. *J. Colloid Sci.* 14:473–91
Galambos PC, Forster F. 1998. An optical micro-fluidic viscometer. In *Micro-Electro-Mechanicical System (MEMS)*, ed. L Lin, NR Aluru, FK Forster, X Zhang, pp. 187–91. New York: Am. Soc. Mech. Eng.
Gauger E, Stark H. 2006. Numerical study of a microscopic artificial swimmer. *Phys. Rev. E* 74:021907
Gittes F, Mickey B, Nettleton J, Howard J. 1993. Flexural rigidity of microtubules and actin filaments measured from thermal fluctuations in shape. *J. Cell Biol.* 120:923–34
Goto S, Nagazono H, Kato H. 1986. The flow behavior of fiber suspensions in Newtonian fluids and polymer solutions. *Rheol. Acta* 25:119–29
Götz T. 2000. *Interactions of fibers and flow: asymptotics, theory and numerics*. PhD Thesis, Univ. Kaiserslautern, Kaiserslautern, Ger.
Goubault C, Leal-Calderon F, Viovy JL, Bibette J. 2005. Self-assembled magnetic nanowires made irreversible by polymer bridging. *Langmuir* 21:3725–29
Griffith B, Hornung R, McQueen D, Peskin C. 2007. An adaptive, formally second order accurate version of the immersed boundary method. *J. Comput. Phys.* 223:10–19
Guazzelli É, Hinch J. 2011. Fluctuations and instability in sedimentation. *Annu. Rev. Fluid Mech.* 43:97–116
Guglielmini L, Kushwaha A, Shaqfeh ES, Stone HA. 2012. Buckling transitions of an elastic filament in a viscous stagnation point flow. *Phys. Fluids* 24:123601
Guo H, Fauci L, Shelley M, Kanso E. 2018. Bistability in the synchronization of actuated microfilaments. *J. Fluid Mech.* 836:304–23
Hämäläinen J, Lindström S, Hämäläinen T, Niskanen H. 2011. Papermaking fibre-suspension flow simulations at multiple scales. *J. Eng. Math.* 71:55–79
Harasim M, Wunderlich B, Peleg O, Kröger M, Bausch AR. 2013. Direct observation of the dynamics of semiflexible polymers in shear flow. *Phys. Rev. Lett.* 110:108302
Haward SJ, Oliveira MS, Alves MA, McKinley GH. 2012. Optimized cross-slot flow geometry for microfluidic extensional rheometry. *Phys. Rev. Lett.* 109:128301
Helgeson ME, Chapin SC, Doyle PS. 2011. Hydrogel microparticles from lithographic processes: novel materials for fundamental and applied colloid science. *Curr. Opin. Colloid Interface Sci.* 16:106–17
Herzhaft B, Guazzelli É. 1999. Experimental study of the sedimentation of dilute and semi-dilute suspensions of fibres. *J. Fluid Mech.* 384:133–58
Hinch E. 1994. Brownian motion with stiff bonds and rigid constraints. *J. Fluid Mech.* 271:219–34
Hirokawa N, Tanaka Y, Okada Y, Takeda S. 2006. Nodal flow and the generation of left-right asymmetry. *Cell* 125:33–45
Huber B, Harasim M, Wunderlich B, Kro M, Bausch AR. 2014. Microscopic origin of the non-Newtonian viscosity of semi flexible polymer solutions in the semidilute regime. *ACS Macro Lett.* 3:136–40
Jawed MK, Khouri NK, Da F, Grinspun E, Reis PM. 2015. Propulsion and instability of a flexible helical rod rotating in a viscous fluid. *Phys. Rev. Lett.* 115:168101
Jeffrey G. 1922. The motion of ellipsoidal particles immersed in a viscous fluid. *Proc. R. Soc. A* 102:161–79
Jeong W, Kim J, Kim S, Lee S, Mensing G, Beebe DJ. 2004. Hydrodynamic microfabrication via "on the fly" photopolymerization of microscale fibers and tubes. *Lab Chip* 4:576–80
Jiang H, Wu Y, Yang B, Zhao YP. 2014. Force–moment line element method for Stokes flow around a slender body. *Eng. Anal. Boundary Elem.* 44:120–29
Johnson R. 1980. An improved slender-body theory for Stokes flow. *J. Fluid Mech.* 99:411–31
Jun Y, Kang E, Chae S, Lee SH. 2014. Microfluidic spinning of micro- and nano-scale fibers for tissue engineering. *Lab Chip* 14:2145–60
Kantsler V, Goldstein RE. 2012. Fluctuations, dynamics, and the stretch-coil transition of single actin filaments in extensional flows. *Phys. Rev. Lett.* 108:038103

Keller J, Rubinow S. 1976. Slender-body theory for slow viscous flow. *J. Fluid Mech.* 75:705–14
Kim MJ, Bird JC, Van Parys AJ, Breuer KS, Powers TR. 2003. A macroscopic scale model of bacterial flagellar bundling. *PNAS* 100:15481–85
Kirchenbuechler I, Guu D, Kurniawan Na, Koenderink GH, Lettinga MP. 2014. Direct visualization of flow-induced conformational transitions of single actin filaments in entangled solutions. *Nat. Commun.* 5:5060
Koens L, Lauga E. 2018. The boundary integral formulation of Stokes flows includes slender-body theory. *J. Fluid Mech.* 850:R1
Kuei S, Słowicka AM, Ekiel-Jezewska ML, Wajnryb E, Stone HA. 2015. Dynamics and topology of a flexible chain: knots in steady shear flow. *New J. Phys.* 17:053009
Lauga E, Powers TR. 2009. The hydrodynamics of swimming microorganisms. *Rep. Prog. Phys.* 72:096601
Li D, Xia Y. 2004. Electrospinning of nanofibers: Reinventing the wheel? *Adv. Mater.* 16:1151
Li L, Manikantan H, Saintillan D. 2013. The sedimentation of flexible filaments. *J. Fluid Mech.* 735:705–36
Lim S, Peskin CS. 2004. Simulations of the whirling instability by the immersed boundary method. *SIAM J. Sci. Comput.* 25:2066–83
Lindner A, Arratia PE. 2016. Preface to special topic: invited articles on microfluidic rheology. *Biomicrofluidics* 10:043301
Ling F, Guo H, Kanso E. 2018. Instability-driven oscillations of elastic microfilaments. arXiv:1808.01583 [physics.flu-dyn]
Liu Y, Chakrabarti B, Saintillan D, Lindner A, du Roure O. 2018. Morphological transitions of elastic filaments in shear flow. *PNAS* 115:9438–43
Machu G, Meile W, Nitsche LC, Schaflinger U. 2001. Coalescence, torus formation and breakup of sedimenting drops: experiments and computer simulations. *J. Fluid Mech.* 447:299–336
Man Y, Page W, Poole RJ, Lauga E. 2017. Bundling of elastic filaments induced by hydrodynamic interactions. *Phys. Rev. Fluids* 2:123101
Manghi M, Schlagberger X, Netz RR. 2006. Propulsion with a rotating elastic nanorod. *Phys. Rev. Lett.* 96:68101
Manikantan H, Li L, Spagnolie SE, Saintillan D. 2014. The instability of a sedimenting suspension of weakly flexible fibres. *J. Fluid Mech.* 756:935–64
Manikantan H, Saintillan D. 2013. Subdiffusive transport of fluctuating elastic filaments in cellular flows. *Phys. Fluids* 25:073603
Manikantan H, Saintillan D. 2015. Buckling transition of a semiflexible filament in extensional flow. *Phys. Rev. E* 92:041002
Manikantan H, Saintillan D. 2016. Effect of flexibility on the growth of concentration fluctuations in a suspension of sedimenting fibers: particle simulations. *Phys. Fluids* 28:013303
Marchetti B, Raspa V, Lindner A, du Roure O, Bergougnoux L, et al. 2018. The deformation of a flexible fiber settling in a quiescent viscous fluid. *Phys. Rev. Fluids.* In press
Mercader C, Lucas A, Derre A, Zakri C, Moisan S, et al. 2010. Kinetics of fiber solidification. *PNAS* 107:18331–35
Metzger B, Guazzelli E, Butler JE. 2005. Large-scale streamers in the sedimentation of a dilute fiber suspension. *Phys. Rev. Lett.* 95:164506
Metzger B, Nicolas M, Guazzelli É. 2007. Falling clouds of particles in viscous fluids. *J. Fluid Mech.* 580:283–301
Mitran SM. 2007. Metachronal wave formation in a model of pulmonary cilia. *Comput. Struct.* 85:763–74
Moeendarbary E, Valon L, Fritzsche M, Harris AR, Moulding DA, et al. 2013. The cytoplasm of living cells behaves as a poroelastic material. *Nat. Mater.* 12:253–61
Morse DC. 1998. Viscoelasticity of concentrated isotropic solutions of semiflexible polymers. 2. Linear response. *Macromolecules* 31:7044–67
Munk T, Hallatschek O, Wiggins CH, Frey E. 2006. Dynamics of semiflexible polymers in a flow field. *Phys. Rev. E* 74:041911
Nagel M, Brun PT, Berthet H, Lindner A, Gallaire F, Duprat C. 2018. Oscillations of confined fibres transported in microchannels. *J. Fluid Mech.* 835:444–70

Nakielski P, Pawłowska S, Pierini F, Liwińska W, Hejduk P, et al. 2015. Hydrogel nanofilaments via core-shell electrospinning. *PLOS ONE* 10:e0129816. Erratum. 2015. *PLOS ONE* 10:e0133458

Nawroth JC, Guo H, Koch E, Heath-Heckman EA, Hermanson JC, et al. 2017. Motile cilia create fluid-mechanical microhabitats for the active recruitment of the host microbiome. *PNAS* 114:9510–16

Nazockdast E, Rahimian A, Needleman D, Shelley M. 2017a. Cytoplasmic flows as signatures for the mechanics of mitotic positioning. *Mol. Biol. Cell* 28:3261–70

Nazockdast E, Rahimian A, Zorin D, Shelley MJ. 2017b. A fast platform for simulating semi-flexible fiber suspensions applied to cell mechanics. *J. Comput. Phys.* 329:173–209

Nguyen H, Fauci L. 2014. Hydrodynamics of diatom chains and flexible fibers. *J. R. Soc. Interface* 11:20140314

Nunes JK, Constantin H, Stone HA. 2013. Microfluidic tailoring of the two-dimensional morphology of crimped microfibers. *Soft Matter* 9:4227–35

Nunes JK, Sadlej K, Tam JI, Stone HA. 2012. Control of the length of microfibers. *Lab Chip* 12:2301–4

Olson SD, Lim S, Cortez R. 2013. Modeling the dynamics of an elastic rod with intrinsic curvature and twist using a regularized stokes formulation. *J. Comput. Phys.* 238:169–87

Park J, Metzger B, Guazzelli É, Butler JE. 2010. A cloud of rigid fibres sedimenting in a viscous fluid. *J. Fluid Mech.* 648:351–62

Pasquali M, Shankar V, Morse DC. 2001. Viscoelasticity of dilute solutions of semiflexible polymers. *Phys. Rev. E* 64:020802

Pawłowska S, Nakielski P, Pierini F, Piechocka IK, Zembrzycki K, Kowalewski TA. 2017. Lateral migration of electrospun hydrogel nanofilaments in an oscillatory flow. *PLOS ONE* 12:e0187815

Perazzo A, Nunes JK, Guido S, Stone HA. 2017. Flow-induced gelation of microfiber suspensions. *PNAS* 114(41):E8557–64

Peskin C. 2002. The immersed boundary method. *Acta Num.* 11:479–517

Pham JT, Lawrence J, Lee DY, Grason GM, Emrick T, Crosby AJ. 2013. Highly stretchable nanoparticle helices through geometric asymmetry and surface forces. *Adv. Mater.* 25:6703–8

Pham JT, Morozov A, Crosby AJ, Lindner A, du Roure O. 2015. Deformation and shape of flexible, microscale helices in viscous flow. *Phys. Rev. E* 92:011004(R)

Pozrikidis C. 1992. *Boundary Integral and Singularity Methods for Linearized Viscous Flow*. Cambridge, UK: Cambridge Univ. Press

Prasath SG, Marthelot J, Govindarajan R, Menon N. 2016. Relaxation of a highly deformed elastic filament at a fluid interface. *Phys. Rev. Fluids* 1:033903

Qian B, Powers T, Breuer K. 2008. Shape transition and propulsive force of an elastic rod rotating in a viscous fluid. *Phys. Rev. Lett.* 100:078101

Qu Z, Temel FZ, Henderikx R, Breuer KS. 2018. Changes in the flagellar bundling time account for variations in swimming behavior of flagellated bacteria in viscous media. *PNAS*. In press

Quennouz N. 2013. *Déformation et transport d'un filament élastique dans un écoulement cellulaire visqueux*. PhD Thesis, Univ. Pierre Marie Curie, Paris, France

Quennouz N, Shelley MJ, du Roure O, Lindner A. 2015. Transport and buckling dynamics of an elastic fiber in a viscous cellular flow. *J. Fluid Mech.* 769:387–402

Ramaswamy S. 2001. Issues in the statistical mechanics of steady sedimentation. *Adv. Phys.* 50:297–341

Reddig S, Stark H. 2011. Cross-streamline migration of a semiflexible polymer in a pressure driven flow. *J. Chem. Phys.* 135:165101

Rusconi R, Lecuyer S, Autrusson N, Guglielmini L, Stone HA. 2011. Secondary flow as a mechanism for the formation of biofilm streamers. *Biophys. J.* 100:1392–99

Rusconi R, Lecuyer S, Guglielmini L, Stone HA. 2010. Laminar flow around corners triggers the formation of biofilm streamers. *J. Roy. Soc. Interface* 7:1293–99

Saad Y, Schultz MH. 1986. GMRES: a generalized minimal residual algorithm for solving nonsymmetric linear systems. *SIAM J. Sci. Stat. Comput.* 7:856–69

Saggiorato G, Elgeti J, Winkler RG, Gompper G. 2015. Conformations, hydrodynamic interactions, and instabilities of sedimenting semiflexible filaments. *Soft Matter* 11:7337–44

Saintillan D, Darve E, Shaqfeh ES. 2005. A smooth particle-mesh Ewald algorithm for Stokes suspension simulations: the sedimentation of fibers. *Phys. Fluids* 17:033301

Schlagberger X, Netz RR. 2005. Orientation of elastic rods in homogeneous Stokes flow. *Europhys. Lett.* 70:129–35. Erratum. 2005. *Europhys. Lett.* 70:563
Schroeder CM, Babcock HP, Shaqfeh ESG, Chu S. 2003. Observation of polymer conformation hysteresis in extensional flow. *Science* 301:1515–19
Sellier A. 1999. Stokes flow past a slender particle. *Proc. R. Soc. Lond. A* 455:2975–3002
Shankar V, Pasquali M, Morse DC. 2002. Theory of linear viscoelasticity of semiflexible rods in dilute solution. *J. Rheol.* 46:1111–54
Shelley MJ. 2016. The dynamics of microtubule/motor-protein assemblies in biology and physics. *Annu. Rev. Fluid Mech.* 48:487–506
Silva PES, Vistulo de Abreu F, Godinho MH. 2017. Shaping helical electrospun filaments: a review. *Soft Matter* 13:6678–88
Słowicka AM, Wajnryb E, Ekiel-Jezewska ML. 2013. Lateral migration of flexible fibers in Poiseuille flow between two parallel planar solid walls. *Euro. Phys. J. E* 36:31
Smith DJ. 2009. A boundary element regularized Stokeslet method applied to cilia- and flagella-driven flow. *Proc. R. Soc. A* 465:3605–26
Son K, Guasto JS, Stocker R. 2013. Bacteria can exploit a flagellar buckling instability to change direction. *Nat. Phys.* 9:494–98
Stein DB, Guy RD, Thomases B. 2017. Immersed boundary smooth extension (IBSE): a high-order method for solving incompressible flows in arbitrary smooth domains. *J. Comput. Phys.* 335:155–78
Steinhauser D, Köster S, Pfohl T. 2012. Mobility gradient induces cross-streamline migration of semiflexible polymers. *ACS Macro Lett.* 1:541–45
Stockie JM, Green SI. 1998. Simulating the motion of flexible pulp fibres using the immersed boundary method. *J. Comput. Phys.* 147:147–65
Strelnikova N, Göllner M, Pfohl T. 2017. Direct observation of alternating stretch-coil and coil-stretch transitions of semiflexible polymers in microstructured flow. *Macromol. Chem. Phys.* 218:1600474
Strychalski W, Copos CA, Lewis OL, Guy RD. 2015. A poroelastic immersed boundary method with applications to cell biology. *J. Comput. Phys.* 282:77–97
Sznitman J, Arratia PE. 2015. Locomotion through complex fluids: an experimental view. In *Complex Fluids in Biological Systems*, ed. S Spagnolie, pp. 245–81. New York: Springer-Verlag
Thomases B, Guy RD. 2017. The role of body flexibility in stroke enhancements for finite-length undulatory swimmers in viscoelastic fluids. *J. Fluid Mech.* 825:109–32
Tornberg A, Gustavsson K. 2006. A numerical method for simulations of rigid fiber suspensions. *J. Comput. Phys.* 215:172–96
Tornberg AK, Shelley M. 2004. Simulating the dynamics and interactions of elastic filaments in Stokes flows. *J. Comput. Phys.* 196:8–40
Trong PK, Doerflinger H, Dunkel J, St Johnston D, Goldstein RE. 2015. Cortical microtubule nucleation can organise the cytoskeleton of *Drosophila* oocytes to define the anteroposterior axis. *eLife* 4:e06088
Wandersman E, Quennouz N, Fermigier M, Lindner A, du Roure O. 2010. Buckled in translation. *Soft Matter* 6:5715–19
Wexler JS, Trinh PH, Berthet H, Quennouz N, du Roure O, et al. 2013. Bending of elastic fibres in viscous flows: the influence of confinement. *J. Fluid Mech.* 720:517–44
Wiens JK, Stockie JM. 2015. Simulating flexible fiber suspensions using a scalable immersed boundary algorithm. *Comput. Methods Appl. Mech. Eng.* 290:1–18
Wiggins CH, Riveline D, Ott A, Goldstein RE. 1998. Trapping and wiggling: elastohydrodynamics of driven microfilaments. *Biophys. J.* 74:1043–60
Wirtz D. 2009. Particle-tracking microrheology of living cells: principles and applications. *Annu. Rev. Biophys.* 38:301–26
Wolgemuth CW, Powers TR, Goldstein RE. 2000. Twirling and whirling: viscous dynamics of rotating elastic filaments. *Phys. Rev. Lett.* 84:1623–26
Wu J, Aidun CK. 2010. A method for direct simulation of flexible fiber suspensions using lattice Boltzmann equation with external boundary force. *Int. J. Multiphase Flow* 36:202–9
Xu X, Nadim A. 1994. Deformation and orientation of an elastic slender body sedimenting in a viscous liquid. *Phys. Fluids* 6:2889–93

Yang Q, Fauci L. 2017. Dynamics of a macroscopic elastic fibre in a polymeric cellular flow. *J. Fluid Mech.* 817:388–405

Young YN. 2009. Hydrodynamic interactions between two semiflexible inextensible filaments in Stokes flow. *Phys. Rev. E* 79:046317

Young YN, Downs M, Jacobs CR. 2012. Dynamics of the primary cilium in shear flow. *Biophys. J.* 103:629–39

Young YN, Shelley M. 2007. A stretch-coil transition and transport of fibers in cellular flows. *Phys. Rev. Lett.* 99:058303

Zhang Q, Zeng S, Lin B, Qin J. 2011. Controllable synthesis of anisotropic elongated particles using microvalve actuated microfluidic approach. *J. Mater. Chem.* 21:2466–69

Zilz J, Schäfer C, Wagner C, Poole RJ, Alves MA, Lindner A. 2014. Serpentine channels: micro-rheometers for fluid relaxation times. *Lab Chip* 14:351–58

Zografos K, Pimenta F, Alves MA, Oliveira MS. 2016. Microfluidic converging/diverging channels optimised for homogeneous extensional deformation. *Biomicrofluidics* 10:043508

Annual Review of
Fluid Mechanics

Volume 51, 2019

Contents

Indexes

Errata

An online log of corrections to *Annual Review of Fluid Mechanics* articles may be found at http://www.annualreviews.org/errata/fluid